

## SWIFT OBSERVATIONS OF MRK 421 IN SELECTED EPOCHS. III. EXTREME X-RAY TIMING/SPECTRAL PROPERTIES AND MULTIWAVELENGTH LOGNORMALITY IN 2015 DECEMBER–2018 APRIL

B. KAPANADZE<sup>1,2,3</sup>, A. GURCHUMELIA<sup>2</sup>, D. DORNER<sup>4</sup>, S. VERCELLONE<sup>3</sup>, P. ROMANO<sup>3</sup>, P. HUGHES<sup>5</sup>, M. ALLER<sup>5</sup>, H. ALLER<sup>5</sup>, O. KHARSHILADZE<sup>6</sup>

*Draft version April 3, 2020*

### ABSTRACT

We present the results from the timing and spectral study of Mrk 421 based mainly on the *Swift* data in the X-ray energy range obtained during the time interval 2015 December–2018 April. The most extreme X-ray flaring activity on the long-term, daily and intraday timescales was observed during the 2-month period which started in 2017 December when the 0.3–10 keV flux exceeded a level of  $5 \times 10^{-9} \text{ erg cm}^{-2} \text{ s}^{-1}$ , recorded only twice previously. While the TeV-band and X-ray variabilities mostly were correlated, the source often varied in a complex manner in the MeV–GeV and radio–UV energy ranges, indicating that the multifrequency emission of Mrk 421 could not be always generated in a single zone. The longer-term flares at X-rays and  $\gamma$ -rays showed a lognormal character, possibly indicating a variability imprint of the accretion disk onto the jet. A vast majority of the 0.3–10 keV spectra were consistent with the log-parabolic model, showing relatively low spectral curvature and correlations between the different spectral parameters, predicted in the case of the first and second-order Fermi processes. The position of the synchrotron spectral energy distribution (SED) peak showed an extreme variability on diverse timescales between the energies  $E_p < 0.1 \text{ keV}$  and  $E_p > 15 \text{ keV}$ , with 15% of the spectra peaking at hard X-rays and was related to the peak height as  $S_p \propto E_p^\alpha$  with  $\alpha \sim 0.6$ , which is expected for the transition from Kraichnan-type turbulence into the “hard-sphere” one. The 0.3–300 GeV spectra showed the features of the hadronic contribution, jet-star interaction and upscatter in the Klein-Nishina regime in different time intervals.

*Keywords:* (galaxies:) BL Lacertae objects: individual: Mrk 421

### 1. INTRODUCTION

Blazars (BL Lacertae objects and flat-spectrum radio quasars) form the most violently variable class of active galactic nuclei (AGNs), with timescales ranging from a few minutes (in the keV–TeV energy range) to several years (radio to optical frequencies). Moreover, BL Lacertae sources (BLLs) are characterized by featureless spectra, variable radio–optical polarization, compact radio-structure and superluminal motion of some components and very broad continuum extending over the radio to the very high-energy (VHE,  $E > 100 \text{ GeV}$ )  $\gamma$ -ray energy ranges. The bolometric luminosity occasionally can reach a level of  $10^{48} \text{ erg s}^{-1}$ , particularly, during the strong outbursts, by the  $\gamma$ -ray emission (see Falomo et al. 2014). Consequently, BLLs are the most frequently detected class of the extragalactic TeV sources (65 out of 82, with redshifts  $z=0.03\text{--}0.61^7$ ) and form one of the most important constituents of LAT 4-year Point Source Catalog (3FGL; Acero et al. 2015). It is widely agreed that the extreme physical properties of BLLs are due to the beamed, non-thermal emission from a relativistic jet which is closely aligned with the observer’s direction (estimated viewing angles  $\theta < 10^\circ$ ) and characterized by the bulk Lorentz factor  $\Gamma \sim 10$ , which occasionally attains values as high as  $\Gamma \sim 50$  (Begelman et al. 2008).

In the  $\log \nu$ – $\log \nu F_\nu$  plane, BLLs generally demon-

strate a double-humped, broadband SED. There is a consensus that the lower-energy component (extended over radio to UV–X-Ray frequencies) is produced by synchrotron emission of ultra-relativistic electrons (Celotti & Ghisellini 2008). A sub-class of the high-energy-peaked BLLs (HBLs, peaking at UV–X-ray frequencies; Padovani & Giommi 1995 and references therein), are particularly important due to the disputed particle acceleration and cooling processes: their X-ray “budget” should be filled by synchrotron photons from the highest-energy leptons (electrons and, possibly, positrons), while the radiative lifetime at these energies are very short (Massaro et al. 2004). Consequently, a detailed study of the timing and spectral behaviour of these sources on diverse timescales reveals the most plausible acceleration mechanisms and allows us to draw conclusions about the physical properties of the jet emission region. Moreover, since the synchrotron and inverse Compton (IC) cooling are expected to be extremely important at these energies, the intense X-ray timing/spectral study of the nearby, bright HBLs may provide us with very important clues about the injection and radiative evolution of the freshly-accelerated particles.

In this regard, the X-ray Telescope onboard the satellite *Swift* (*Swift*-XRT; Burrows et al. 2005) makes an outstanding contribution by performing a regular monitoring of selected BLLs in their “visibility” periods, particularly, during the densely-sampled Target of Opportunity (TOO) observations<sup>8</sup>. Owing to the excellent instrumental characteristics, good photon statistics and low background counts of *Swift*-XRT, we are able to search for flux and spectral variability on diverse time-scales (minutes to years), obtain high-quality spectra and derive different spectral parameters for bright HBLs even for exposures lasting a few hundred seconds.

The nearby ( $z=0.031$ ), TeV-detected HBL source

<sup>1</sup> Iliia State University, Colokashvili Av. 3/5, Tbilisi, Georgia, 0162.

<sup>2</sup> E. Kharadze National Astrophysical Observatory, Mt. Kanobili, Abastumani, Georgia, 0803

<sup>3</sup> INAF, Osservatorio Astronomico di Brera, Via E. Bianchi 46, 23807 Merate, Italy.

<sup>4</sup> Universität Würzburg, Institute for Theoretical Physics and Astrophysics, Emil-Fischer-Str. 31, 97074 Würzburg, Germany

<sup>5</sup> Astronomy Department, University of Michigan, Ann Arbor, MI 48109-1107, USA

<sup>6</sup> I. Javakhishvili State University, Chavchavadze Av. 3, Tbilisi 0128, Republic of Georgia

<sup>7</sup> <http://tevcat.uchicago.edu/>

<sup>8</sup> <https://www.swift.psu.edu/toop/toop.php>

**Table 1**

The intervals and sub-intervals referred throughout the paper.

Period	Dates	MJD
1	2015 December 8 to 2016 June 16	57364–57555
1a	2015 December 8 to 2016 February 4	57364–57422
1b	2016 February 6 to 2016 June 16	57424–57555
2	2016 November 25 to 2017 June 27	57717–57931
2a	2016 November 25 to 2017 January 29	57717–57782
2b	2017 January 31 to 2017 June 27	57784–57931
3	2017 December 3 to 2018 April 8	58090–58216
3a	2017 December 16 to 2018 February 19	58103–58168
3b	2018 February 21 to 2018 April 8	58170–58216

Mrk 421 provides an unique X-ray space laboratory due to the features as follows (Balokovic et al. 2016; Kapanadze et al. 2016, 2018a,b): (i) high brightness (with the *Swift*-XRT 0.3–10 keV count rates  $CR > 100 \text{ cts s}^{-1}$  during strong flares, corresponding to de-absorbed fluxes  $F_{0.3-10\text{keV}} \gtrsim 2.5 \times 10^{-9} \text{ erg cm}^{-2} \text{ s}^{-1}$ ; ; (ii) exceptionally strong outbursts (e.g., in 2013 April; Pian et al. 2014; Kapanadze et al. 2016); (iii) very large and fast timing/spectral variability on timescales down to a few hundred seconds; (iv) extremely hard spectra during strong flares with the photon index smaller than 1.6 and synchrotron SED peak shifting beyond 10 keV etc. Moreover, the source is also bright in other spectral ranges, making it a frequent target of densely-sampled MWL campaigns (Macomb et al. 1995, Aleksic et al. 2012, 2015a,b, Balokovic et al. 2016 etc.), which are crucial for checking the viability of models explaining the origin of the higher-energy SED component via the inter-band correlation study: (1) synchrotron self-Compton (SSC, scattering of synchrotron photons by their “parent” lepton population; Marscher & Gear 1985); (2) external Compton (EC), with the low-energy photons from the accretion disc (AD), dust torus, narrow/broad line clouds upscattered by the jet ultra-relativistic particles (Dermer et al. 1992); (3) hadronic models, which embody a generation of the keV–TeV emission by relativistic protons, either directly (synchrotron-proton scenario; Abdo et al. 2011) or indirectly (e.g., synchrotron radiation by the electron population, produced by a cascade induced by the interaction of high-energy protons with the ambient photons; Mannheim 1993). Despite the large number of publications related to the aforementioned observations, the details of the physical processes underlying the higher-energy SED component remain mainly unknown owing to (i) sparse multiwavelength (MWL) data during long periods; (ii) moderate or low sensitivity in the hard X-ray and  $\gamma$ -ray energy ranges in the past; (iii) many previous MWL campaigns were triggered in the epochs of enhanced X-ray and  $\gamma$ -ray activity, and, consequently, these studies are biased towards the high states of the source, while the distinct physical processes may play a dominant role during the moderate and lower brightness states.

For the aforementioned reasons, we performed a detailed study of X-ray spectral and flux variability in the MWL context, focussed on the rich archival data obtained with XRT during 2005 March–2015 June (Kapanadze et al. 2016, 2017a, 2018a,b). This campaign revealed extreme X-ray flares by a factor of 3–20 on the timescales of a few days–weeks between the lowest historical state and that corresponding to the *Swift*-XRT rate higher than  $200 \text{ cts s}^{-1}$ . The source was characterized by extreme spectral and intraday flux variability, particularly during the strong flares. In the latter case, we were able to extract the 0.3–10 keV spectra for the time intervals of 50–100 seconds and explore the observational

acceleration and emission scenarios. The distribution of different spectral parameters and their cross-correlations hinted at the importance of the first and second-order Fermi accelerations, changes in the turbulence type, possible hadronic contribution to the MeV–GeV emission etc.

In this paper, we present the results of our detailed study of the timing/spectral behaviour of Mrk 421 during the period 2015 December–2018 April, which was characterized by a very strong X-ray flare in the time interval 2017 December–2018 February, and showed an intensive flaring activity also in other parts of the here-presented period, revealed by the densely-sampled *Swift*-XRT observations. Using XRT observations, we checked correlations between the 0.3–10 keV flux variability and those observed with different instruments: the Ultraviolet-Optical Telescope (UVOT; Roming et al. 2005) and the Burst Alert Telescope (BAT; Barthelmy et al. 2005) onboard *Swift*, the Large Area Telescope (LAT) onboard *Fermi* (Atwood et al. 2009), MAXI (Matsuoka et al. 2009), the First G-APD Cherenkov Telescope (FACT; Anderhub et al. 2013), the 40-m telescope of Owens Valley Radio Observatory (OVRO; Richards et al. 2011), the optical telescopes of Steward Observatory (Smith et al. 2009).

The paper is organized as follows: Section 2 encompasses the description of the data processing and analyzing procedures. The results of the X-ray and MWL timing study, as well as those from the X-ray spectral analysis are presented in Section 3. We provide a discussion, based on our results, and the corresponding conclusions in Section 4. Finally, the summary of our study is given in Section 5.

## 2. DATA SETS, REDUCTION AND ANALYSIS

### 2.1. X-Ray Data

We retrieved the raw *Swift*-XRT data from *NASA’s Archive of Data on Energetic Phenomena*<sup>9</sup> (HEASARC). The Level 1 event files were reduced, calibrated and cleaned via the `XRTPIPELINE` script (included in the package `HEASOFT v. 6.26`) by applying the standard filtering criteria and the latest calibration files of XRT CALDB v.20190412. The events with 0-2 grades are selected for those observations performed in the Windowed Timing (WT) mode. The selection of the source and background extraction regions was performed with `XSELECT`, using the circular area with radii of 25–50 pixels depending on the source brightness and position in the XRT field-of view (FOV), as well as on the exposure length. We produced a pile-up correction for the count rate  $CR \gtrsim 100 \text{ cts s}^{-1}$  by excluding the central area with radii of 1–3 pixels from the source extraction region, following the recipe provided by Romano et al. (2006). Afterwards, the light curves were corrected using the task `XRTLCCORR` for the resultant loss of the effective area, bad/hot pixels, pile-up, and vignetting. Moreover, the corrections on the point-spread function losses, different extraction regions, vignetting and CCD defects were done by generating the ancillary response files (ARFs) using the `XRTMKARF` task.

Due to the high X-ray brightness of the source, it generally was not observed in the Photon Counting (PC) regime. However, Mrk 421 was accidentally targeted in this regime three times in the here-presented period (ObsIDs 35014255<sup>10</sup>, 34228023 and 34228026). In those cases, we used the events with 0-12 grades for our analysis. The pile-up correction was done according to the pre-

<sup>9</sup> <https://heasarc.gsfc.nasa.gov/>

<sup>10</sup> The three leading zeroes of each ObsID are omitted throughout the paper.

**Table 2**

Summary of the XRT and UVOT observations in the time interval 2015 December–2018 April (extract; see the corresponding machine-readable table for the entire content). The columns are as follows: (1) – observation ID; (2) – observation start–end; (3) – Modified Julian date corresponding to the observation start; (4) exposure (in seconds); (5) observation-binned 0.3–10 keV count rate and the associated uncertainty shown within parentheses; (6) – (11) – de-reddened UVOT magnitudes and corresponding fluxes (in mJy).

ObsID	Obs. Start – End (UTC)	MJD	Exp. (s)	CR (cts s <sup>-1</sup> )	UVW1 (mag)	UVW1 (mJy)	UVM2 (mag)	UVM2 (mJy)	UVW2 (mag)	UVW2 (mJy)
(1)	(2)	(3)	(4)	(5)	(6)	(7)	(8)	(9)	(10)	(11)
35014240	2015-12-08 10:15:58–11:22:39	57364.431	1015	7.11(0.09)	11.53(0.11)	21.79(0.79)	11.72(0.04)	15.65(0.28)	11.51(0.10)	18.31(0.46)
35014241	2015-12-11 11:38:58–12:43:43	57367.487	959	21.14(0.15)	11.78(0.10)	17.29(0.63)	11.90(0.04)	13.25(0.28)	11.80(0.03)	14.00(0.28)
35014242	2015-12-14 09:56:58–11:02:04	57370.416	1069	49.04(0.22)	11.47(0.11)	23.03(0.79)	11.67(0.04)	16.39(0.28)	11.47(0.10)	18.99(0.46)
35014243	2015-12-17 11:20:58–12:26:26	57373.475	1015	43.58(0.21)	11.54(0.11)	21.59(0.79)	11.76(0.04)	15.09(0.28)	11.49(0.10)	18.65(0.46)
35014245	2015-12-18 04:50:58–23:29:49	57374.204	5892	29.34(0.14)	11.49(0.10)	22.61(0.74)	11.66(0.10)	16.55(0.38)	11.50(0.10)	18.48(0.41)

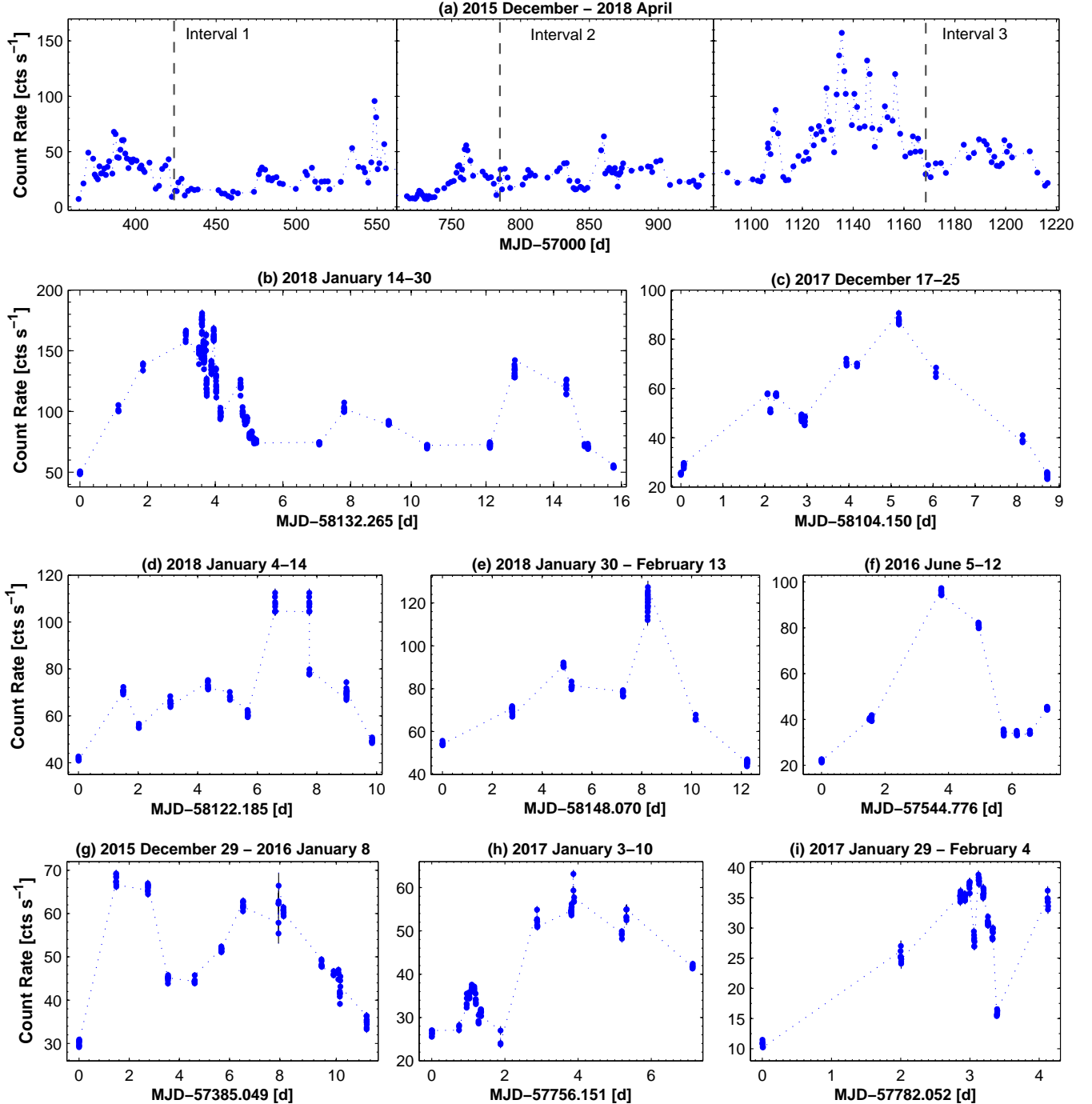


**Figure 1.** Panel (a): X-ray flaring activity of Mrk 421 in the 0.3–10 keV energy range during different periods. In each plot, the vertical dashed line denotes a boundary between the different sub-intervals; panels (b)–(i): the strongest X-ray flares during Intervals 1–3.

scription of Moretti et al. 2005. The radius, below which the model overproduced the data, was accepted as a region affected by pile-up (11–15 pixels for the particular observation). The source events were extracted from an annular region with the inner radius coinciding the pile-up

area and the outer radius of 50–60 pixels. The loss of counts caused by the inner hole in the source region, vignetting and bad pixels were corrected by generating the corresponding ARF-file. The background counts were extracted from a corresponding annulus with radii of 80 and

**Table 3**

Summary of the XRT and UVOT observations in different intervals. Cols (2)–(5): maximum 0.3–10 keV flux (in  $\text{cts s}^{-1}$ ), maximum-to-minimum flux ratio, mean flux and fractional amplitude, respectively; maximum de-absorbed flux (in  $10^{-10} \text{ erg cm}^{-2} \text{ s}^{-1}$ ), maximum-to-minimum flux ratio, mean flux and fractional amplitude in the 0.3–2 keV (Cols (6)–(9)) and 2–10 keV (Cols (10)–(13)) bands; maximum unabsorbed flux (in mJys), maximum-to-minimum flux ratio and fractional amplitude in the bands UVW1 (Cols (15)–(18)), UVM2 (Cols (19)–(22)) and UVW2 (Cols (23)–(26)).

XRT												
0.3–10 keV					0.3–2 keV				2–10 keV			
Per.	$CR_{\text{max}}$	$\mathfrak{R}$	Mean	$100 \times F_{\text{var}}$	$F_{\text{max}}$	$\mathfrak{R}$	Mean	$100 \times F_{\text{var}}$	$F_{\text{max}}$	$\mathfrak{R}$	Mean	$100 \times F_{\text{var}}$
(1)	(2)	(3)	(4)	(5)	(6)	(7)	(8)	(9)	(10)	(11)	(12)	(13)
1	95.72(0.32)	13.5	31.53(0.02)	50.5(0.1)	15.85(0.18)	12.3	7.19(0.01)	41.6(0.1)	13.93(0.38)	59.5	3.55(0.01)	75.0(0.2)
1a	67.83(0.28)	9.5	37.98(0.03)	35.4(0.1)	12.76(0.26)	9.9	7.60(0.01)	30.3(0.1)	7.96(0.24)	34.0	3.31(0.01)	44.5(0.3)
1b	95.72(0.32)	11.4	26.56(0.03)	60.3(0.1)	15.85(0.18)	8.3	6.62(0.01)	55.9(0.1)	13.93(0.38)	46.3	38.90(0.01)	95.9(0.4)
2	63.75(0.30)	9.0	25.81(0.02)	44.5(0.1)	12.02(0.14)	7.9	5.54(0.01)	34.2(0.1)	12.25(0.33)	47.5	38.24(0.01)	58.8(0.2)
2a	55.70(0.18)	7.9	21.40(0.03)	62.4(0.1)	9.66(0.15)	6.4	5.45(0.01)	39.7(0.1)	9.33(0.25)	36.2	37.70(0.01)	65.8(0.4)
2b	63.75(0.30)	4.2	28.43(0.03)	33.5(0.1)	12.02(0.14)	4.2	5.61(0.01)	30.1(0.1)	12.25(0.33)	12.7	38.62(0.01)	53.9(0.3)
3	162.88(0.70)	8.5	60.89(0.03)	51.0(0.1)	26.85(0.30)	13.2	14.29(0.01)	38.8(0.01)	29.04(0.79)	31.2	11.80(0.02)	63.4(0.2)
3a	162.88(0.70)	7.1	71.26(0.04)	45.9(0.1)	26.85(0.30)	6.1	15.60(0.01)	33.5(0.01)	29.04(0.79)	22.1	13.30(0.02)	55.6(0.2)
3b	61.10(0.26)	3.2	43.33(0.05)	27.2(0.1)	19.45(0.27)	9.6	8.52(0.01)	38.5(0.02)	10.38(0.32)	11.1	5.15(0.02)	40.4(0.4)

UVOT												
UVW1				UVM2				UVW2				
Per.	$F_{\text{max}}$	$\mathfrak{R}$	Mean	$100 \times F_{\text{var}}$	$F_{\text{max}}$	$\mathfrak{R}$	Mean	$100 \times F_{\text{var}}$	$F_{\text{max}}$	$\mathfrak{R}$	Mean	$100 \times F_{\text{var}}$
(14)	(15)	(16)	(17)	(18)	(19)	(20)	(21)	(22)	(23)	(24)	(25)	(26)
1	29.83(1.05)	2.4	22.8(0.4)	20.36(0.07)	21.22(0.41)	2.1	15.19(0.03)	21.3(0.2)	26.24(0.74)	2.4	18.10(0.05)	23.0(0.3)
1a	28.75(0.97)	1.7	22.86(0.13)	12.5(0.6)	20.64(0.28)	1.7	15.88(0.04)	16.5(0.3)	26.24(0.74)	1.9	20.09(0.07)	15.1(0.4)
1b	29.83(1.05)	2.4	18.15(0.09)	26.5(0.5)	21.22(0.41)	2.1	14.55(0.03)	25.0(0.3)	25.06(0.64)	2.3	16.16(0.06)	26.1(0.4)
2	18.11(0.63)	2.1	11.33(0.04)	18.4(0.3)	11.11(0.19)	2.7	7.73(0.02)	20.0(0.2)	14.13(0.28)	1.9	9.90(0.02)	14.9(0.2)
2a	18.11(0.63)	2.1	12.8(0.07)	19.9(0.6)	11.11(0.19)	2.7	7.56(0.03)	28.2(0.4)	14.13(0.28)	1.9	10.65(0.04)	17.1(0.4)
2b	13.71(0.50)	1.5	10.38(0.04)	7.9(0.04)	10.51(0.19)	1.9	7.84(0.02)	13.1(0.3)	13.00(0.28)	1.7	9.42(0.03)	10.1(0.3)
3	25.50(0.64)	2.1	19.40(0.07)	20.1(0.4)	18.82(0.28)	2.0	13.6(0.03)	17.2(0.2)	22.43(0.56)	2.0	17.16(0.04)	19.0(0.3)
3a	25.50(0.64)	1.4	21.82(0.10)	7.2(0.5)	18.82(0.28)	1.6	14.92(0.04)	10.8(0.3)	22.43(0.56)	1.4	19.29(0.06)	7.1(0.3)
3b	19.14(0.63)	1.6	14.10(0.10)	14.8(0.7)	15.08(0.28)	1.6	11.17(0.04)	12.1(0.4)	17.64(0.41)	1.6	12.99(0.06)	13.1(0.5)

120 pixels.

From the publicly available, daily-binned BAT<sup>11</sup> and MAXI<sup>12</sup> data, we used only those corresponding to the target’s detection with a minimum significance of  $5\sigma$  to study a variability of the 15–150 keV and 2–20 keV fluxes, respectively.

## 2.2. $\gamma$ -ray Observations

The reduction of the *Fermi*–LAT data was performed with *ScienceTools* (version v11r5p3), adopting the instrument response function P8R3\_SOURCE\_V2 and the unbinned maximum likelihood method GTLIKE. We selected the 0.3–300 GeV energy range for extraction of the photon flux and spectral information, since the effective area of the instrument is larger ( $>0.5 \text{ m}^2$ ) and the angular resolution relatively good (the 68% containment angle smaller than 2 deg) in that case (Atwood et al. 2009). Consequently, we obtain smaller systematic errors and the spectral fit is less sensitive to possible contamination from unaccounted, transient neighbouring sources (Abdo et al. 2011). The events of the diffuse class (`evclass=128`, `evtype=3`), i.e. those with the highest probability of being photons, from a region of interest (ROI) with the 10-deg radius centered at the location of Mrk 421 were included in our analysis. Moreover, we discarded the events at zenith angles  $>100$  deg (to avoid a contamination from the Earth-albedo photons, generated by cosmic rays interacting with the upper atmosphere) and those recorded when the spacecraft rocking angle was larger than 52 deg (greatly reducing the contamination from Earth-limb photons).

The background model `gll_iem_v07.fits` was created to extract the  $\gamma$ -ray signal from (i) the Galactic diffuse-emission component; (ii) an isotropic component, which is the sum of the extragalactic diffuse emission and the residual charged particle background (parameterized

by the file `iso_P8R3_SOURCE_V2_v1.txt`); (iii) all  $\gamma$ -ray sources from the *Fermi*–LAT 4-yr Point Source Catalog (3FGL, Acero et al. 2015) within 20 deg of Mrk 421. For the spectral modelling of our target, we adopted a simple power law, similar to the 3FGL catalogue. The spectral parameters of the sources within the ROI were left free during the minimization process while those outside of this range were held fixed to the 3FGL catalog values. The normalizations of both components (i)–(ii) in the background model were allowed to vary freely during the spectral fit. The photon flux and spectral parameters were estimated using the unbinned maximum-likelihood technique (Mattox et al. 1996).

When the target’s detection significance is less than  $5\sigma$  (i.e., the corresponding test-statistics  $TS < 25$ ) and/or the number of the model-predicted counts  $N_{\text{pred}} \lesssim 10$ , such detections are not robust. For example, even a small change in the time-bin width can result in significantly different values of the photon flux and spectral parameters. In such cases, we calculated the upper limit to the photon flux<sup>13</sup>.

We used the user-contributed tool `likeSED`<sup>14</sup> to construct the 300 MeV–300 GeV SED of Mrk 421. In that case, the photon indices of the sources were frozen to the best-fit values obtained from the full spectral analysis when performing unbinned likelihood fits in differential energy bins (following the recipe provided in Aleksic et al. 2015a).

The source was observed with FACT at VHE energies during 363 nights for a total of 1408 hr in the period 2015 December 8–2018 April 8. For the timing study, we have used only the nightly-binned TeV excess rates corresponding to detection significances higher than  $3\sigma$ <sup>15</sup>, since more than 98% of these data are taken with a zenith distance small enough to not influence significantly the

<sup>11</sup> <http://swift.gsfc.nasa.gov/results/transients/weak/Mrk421/>

<sup>12</sup> <http://maxi.riken.jp/>

<sup>13</sup> See [fermi.gsfc.nasa.gov/ssc/data/analysis/scitools/upper\\_limits.html](http://fermi.gsfc.nasa.gov/ssc/data/analysis/scitools/upper_limits.html)

<sup>14</sup> <https://fermi.gsfc.nasa.gov/ssc/data/analysis/user/>

<sup>15</sup> See <http://www.fact-project.org/monitoring/>

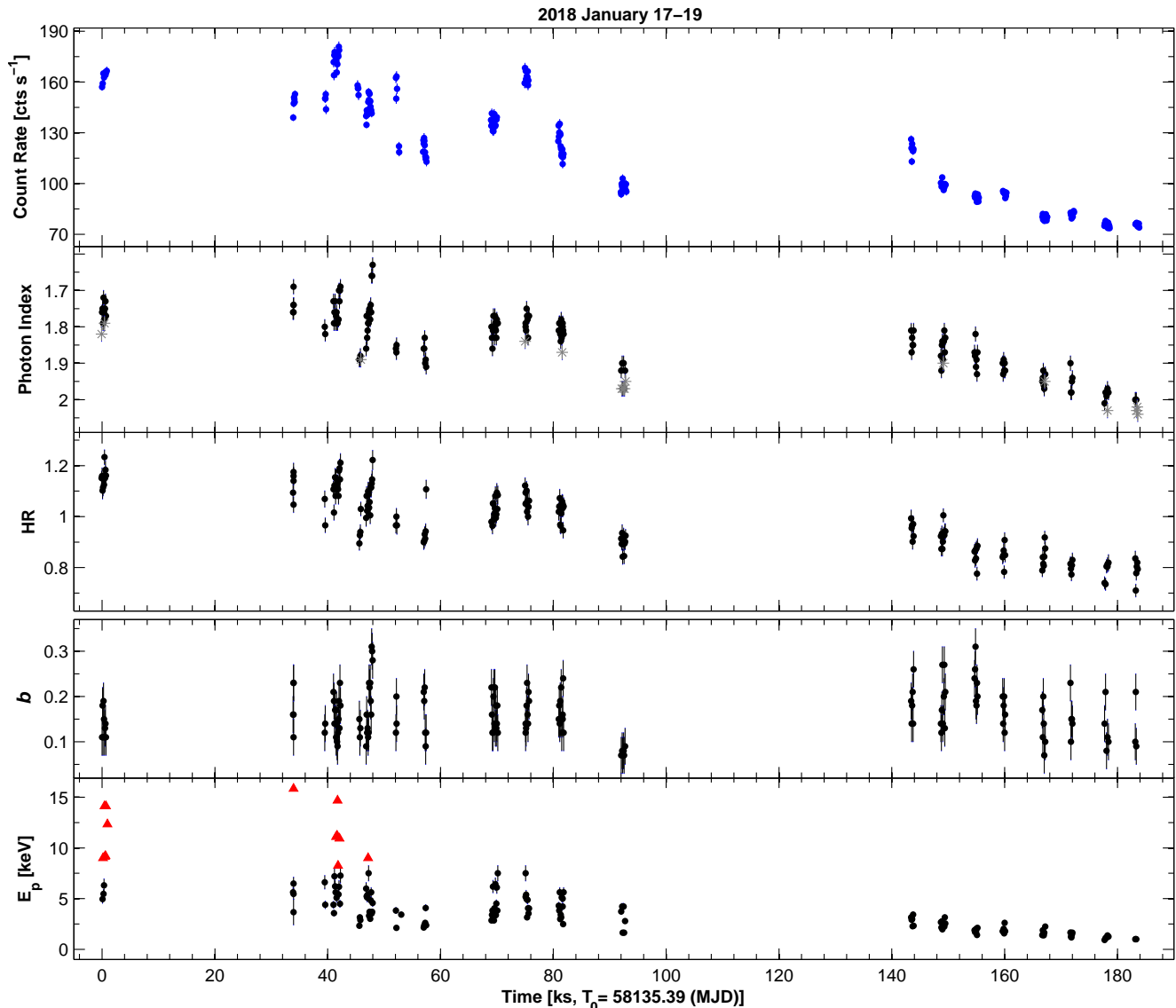


**Figure 2.** Top panel: intraday 0.3–10 keV variability during the strongest X-ray flaring activity in 2018 January 17–19. The subsequent panels: timing behaviour of different spectral parameters. In the second panel, the black points and the gray asterisks stand for the photon indices  $a$  and  $\Gamma$ , respectively. Red triangles in the bottom panel stand for the lower limits to the intrinsic position of the synchrotron SED peak.

energy threshold of the analysis (see Dorner et al. 2015 for the data reduction and analysis details). More than 84% of the same data are taken under light conditions not increasing the analysis threshold. This results in 190 nights for which the nightly observation time ranges of 0.66–7.32 hr. In the case of the 20-min binned data, the source was detected 456-times in the here-presented period, and the corresponding rates were used in searching for the intraday brightness variability.

### 2.3. UV, Optical and radio data

The source was targeted with *Swift*-UVOT in the ultraviolet bands *UVW1*, *UVM2*, and *UVW2* simultaneously with XRT. Generally, Mrk 421 was not observed with UVOT in the optical *V–U* bands due to the presence of very bright stars in the telescope’s FOV. The absolute photometry for the sky-corrected images was performed by means of the *UVOTSOURCE* tool (distributed within *HEASOFT*) and the calibration files included in the CALDB v.20170922. The measurements were done using a 20 arcsec radius due to the target’s high UV-brightness. When the source was brighter than 12 mag, a pile-up was estimated and the corresponding correction was performed using the recipe provided in Page et al. (2013). According to the latter, a systematic uncertainty

magnitudes were then corrected for the Galactic absorption adopting  $E(B-V)=0.028$  mag (see Kapanadze et al. 2018a), and the  $A_{\lambda}/E(B-V)$  values derived from the interstellar extinction curves (Fitzpatrick & Massa 2007). For this purpose, we used the effective wavelength of each filter adopted from Poole et al. (2008). Finally, the magnitudes were converted into milli-Janskys by adopting the latest photometric zero-points for each band provided in Breeveld et al. (2011), and the host contribution was removed by subtracting the values of 0.09 mJy, 0.05 mJy and 0.06 mJy for the *UVW1*, *UVM2*, *UVW2* bands, respectively (Cesarini 2012).

The publicly available *V* and *R*-band magnitudes, obtained with the 2.3 m Bock and 1.54 m Kuiper telescopes of Steward observatory<sup>16</sup> (see Smith et al. 2009 for details), were de-reddened and converted into milli-Janskys according to Bessel (1979). In both bands, the host contribution was subtracted following Nilsson et al. (2007) and Fukugita et al. (1995).

The 15 GHz radio fluxes, obtained with the OVRO 40-m telescope, were retrieved from the corresponding website<sup>17</sup> (see Richards et al. 2011 for the data reduction and calibration steps). The sharp spikes or drops in the light

<sup>16</sup> See <http://james.as.arizona.edu/~psmith/Fermi/>

<sup>17</sup> see <http://www.astro.caltech.edu/ovroblzars/>

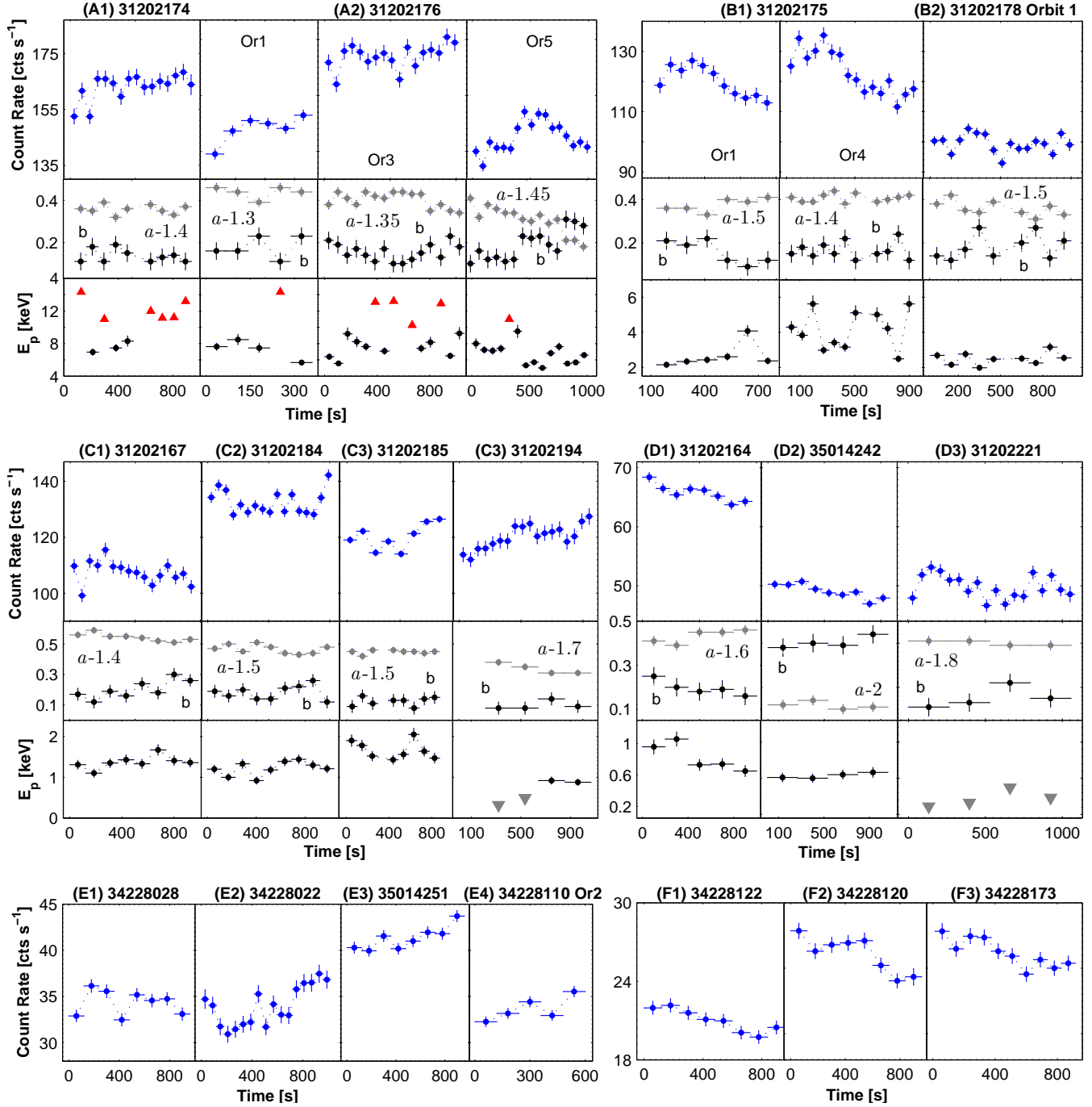


**Figure 3.** The fastest 0.3–10 keV IDVs. In the second panel of Figures A1–D3, the gray points correspond to the photon index  $a$ , arbitrarily shifted for the better resolution. The red and gray triangles in the bottom panels of (A1)–(A2), (C3) and (D3) plots stand for the lower and upper limits to the intrinsic position of the synchrotron SED peak, respectively.

curve, associated with less-favourable observing conditions, were not included in our analysis.

#### 2.4. Analysis Methods

The 0.3–10 keV spectra, extracted from the XRT observations and corrected for the different effects (see Section 2.1), were further reduced as follows: using the GRPPHA task, we combined the instrumental channels to include at least 20 photons per bin, making a spectrum valid for the  $\chi^2$ -statistics. The reduced spectra were fitted with three different models, generally adopted for the blazar X-ray spectra (by fixing the Hydrogen column density to the Galactic value  $N_{\text{H}} = 1.90 \times 10^{20} \text{ cm}^{-2}$ , obtained within the Leiden/Argentine/Bonn (LAB) survey; Kalberla et al. 2005): (1) log-parabolic model (Massaro et al. 2004)

with  $E_1$  fixed to 1 keV;  $a$ , the photon index at the energy  $E_1$ ;  $b$ , the curvature parameter;  $K$ , the normalization factor. The position of the synchrotron SED peak was calculated as  $E_p = 10^{(2-a)/2b}$  keV; (2) simple power-law  $F(E) = KE^{-\Gamma}$ , with  $\Gamma$ , the photon index throughout the entire 0.3–10 keV energy range; (3) broken power-law

$$F(E) = \begin{cases} KE^{-\Gamma_1}, & E \leq E_{\text{br}} \\ KE_{\text{br}}^{\Gamma_2 - \Gamma_1} (E/1\text{keV})^{-\Gamma_2}, & E > E_{\text{br}}, \end{cases} \quad (2)$$

with  $E_{\text{br}}$ : break point for the energy in keV,  $\Gamma_1$ : photon index for  $E \leq E_{\text{br}}$ ,  $\Gamma_2$ : photon index for  $E > E_{\text{br}}$ . The model validity was determined using the reduced chi-squared ( $\chi_r^2$ ), distribution of the residuals, and F-test. The high X-ray brightness of Mrk 421 allowed us to extract the spectra from separate orbits of the particular ObsID (especially important when it is impossible to use

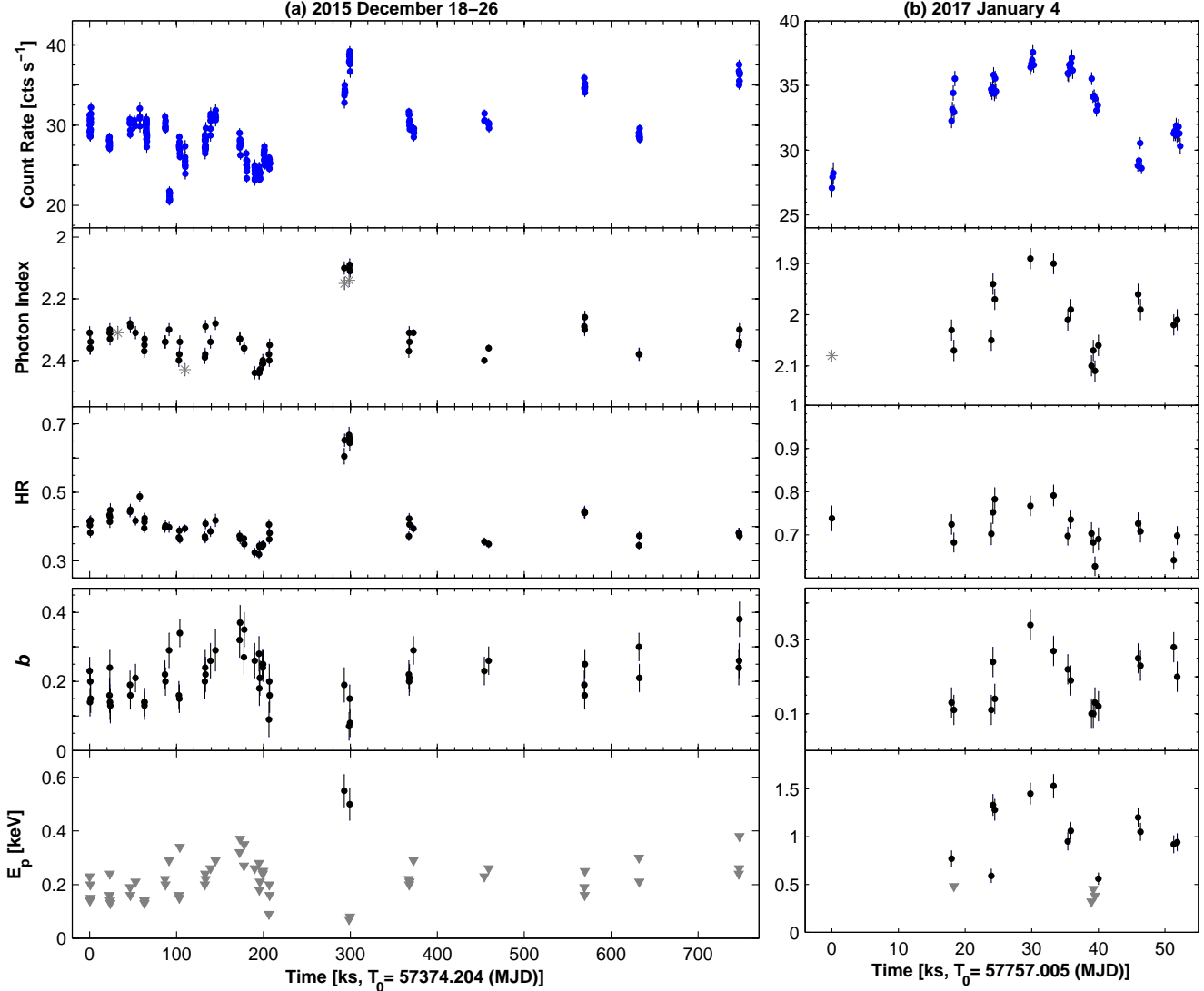


**Figure 4.** Two examples of the densely sampled 0.3–10 keV light curves with a weaker intraday variability. In the second panel, the black points and the gray asterisks stand for the photon indices  $a$  and  $\Gamma$ , respectively. Gray triangles in the bottom panel stand for the upper limits to the intrinsic position of the synchrotron SED peak.

**Table 4**

The 0.3–10 keV IDVs during 2015 December–2018 April (extract; see the corresponding machine-readable table for the full version). Col. (1) contains the ObsIDs of those *Swift*-XRT pointings to the source during which the given event was recorded. Col. (2) presents the MJD of the observation start and the total length of the particular observation (including the intervals between the separate orbits); Col. (3): reduced chi-squared and the corresponding degrees-of-freedom for the given observations, along with the time bin used for the variability search; Col. (4): fractional variability amplitude and the associated error in the parenthesis; Cols (5)–(8): the ranges of different spectral parameters, obtained via the log-parabolic (LP) or power-law (PL) fits with the spectra extracted from the separate orbits (or segments) of the corresponding XRT observation. The last column provides a remark related to the variable spectral parameter making the basic contribution in the observed IDV: 1 – photon index; 2 – curvature; 3 –  $E_p$ ; 4 –  $S_p$ ; 5 – change in the particles’ energy distribution from the log-parabolic functional shape into the power-law one or vice versa.

ObsID(s) (1)	MJD/ $\Delta T$ (hr) (2)	$\chi_r^2/\text{dof}/\text{bin}$ (3)	$100 \times F_{\text{var}}$ (4)	$a$ or $\Gamma$ (5)	$b$ (6)	$E_p$ (keV) (7)	HR (8)	Remark (9)
35014242	57370.416/0.30	3.41/8/120 s	2.1(0.5)	2.20(0.02)–2.24(0.02)	0.38(0.04)–0.44(0.04)	0.50(0.06)–0.58(0.07)	0.41(0.01)–0.44(0.02)	1
34014243– 31202245 Or1	57373.475/17.98	2925/1/Or	26.3(0.3)	2.17(0.02)–2.31(0.02)	0.20(0.05)–0.27(0.05)	0.21(0.04)–0.48(0.06)	0.38(0.01)–0.51(0.02)	1,3
35014245	57374.204/18.66	28.63/5/Or	3.4(0.3)	2.28(0.02)–2.36(0.02) LP 2.31(0.02) PL	0.13(0.04)–0.23(0.04)	0.05(0.02)–0.24(0.05)	0.38(0.01)–0.45(0.02)	1,2,4,5
35014245 Or1	57374.204/0.48	2.82/18/90 s	2.7(0.5)	2.31(0.02)–2.36(0.02)	0.14(0.04)–0.23(0.04)	0.05(0.02)–0.21(0.04)	0.38(0.01)–0.42(0.02)	1,2,4

for all orbits, or the source is variable), or even from the separated segments of a single orbit in the medium and higher brightness states. The unabsorbed 0.3–2 keV, 2–10 keV and 0.3–10 keV fluxes and their errors (in logarithmic units) were derived using the task EDITMOD.

The hardness ratio (HR) was determined as  $HR = F_{2-10 \text{ keV}} / F_{0.3-2 \text{ keV}}$  where the symbols  $F_{2-10 \text{ keV}}$  and  $F_{0.3-2 \text{ keV}}$  stand for the de-absorbed 2–10 keV to 0.3–2 keV fluxes, respectively.

In order to study the statistical properties of different

spectral parameters, we constructed a histogram and normalized cumulative distribution for the values of each parameter. A Kolmogorov-Smirnov (K-S) test was adopted to compare the distributions of the particular parameter in different time intervals, defined in Table 1, and to measure the distance  $D_{K-S}$  between the normalized cumulative distributions of parameters corresponding to the two different periods, following the recipe provided by Massaro et al. (2011a). Since our samples are not statistically complete, a comparison of the correspond-

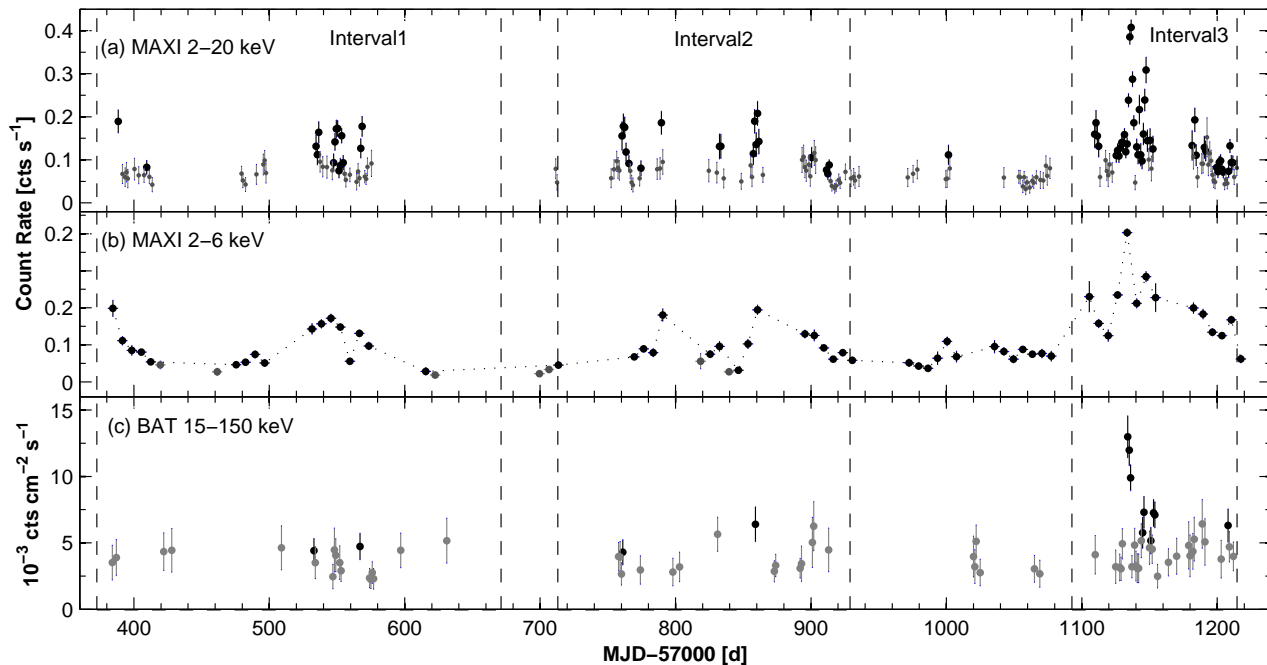


**Figure 5.** Long-term behaviour of Mrk 421 in the MAXI 2–20 keV and 2–6 keV bands (panels (a) and (b), respectively), as well as in the BAT energy range (bottom panel). The daily-binned data are used to construct light curves. The black and gray points correspond to the detections with  $5\sigma$  and  $3\sigma$  significances, respectively.

ing distributions can be affected by biases and there is a risk of obtaining a large  $D_{K-S}$  value between the selected cumulative distributions indicating that they are different, simply due to the lack/absence of the data in some particular bins of each histogram. To check the significance of the results provided by the K-S test, we adopted a method based on the Monte Carlo simulations (developed by Massaro et al. 2011a) to account for this effect and estimate its relevance: firstly, we performed the K-S test and derived the  $D_{K-S}$  quantity for two normalized cumulative distributions. Afterwards, we randomly simulated two distributions for both data sets with the same number of components, adopting two different shapes for the simulated distributions: log-uniform and lognormal - the former having simply the same maximum and minimum values of the observed distribution, while the latter with the same variance, the same median of the observed distribution and spanning the same range of values. We measured the  $D_{K-S, \text{simul}}$  distance between the simulated distributions, repeated simulations at least 30000 times and built a distribution of the obtained  $D_{K-S, \text{simul}}$ . Finally, we estimated the probability of obtaining the observed  $D_{K-S}$  randomly, that provides the confidence level of our K-S test.

For each variability instance, we calculated the fractional variability amplitude and its error according to Vaughan et al. (2003)

$$F_{\text{var}} = (S^2 - \overline{\sigma_{\text{err}}^2})^{1/2} / \overline{F}$$

$$\text{err}(F_{\text{var}}) = \left\{ \left( \sqrt{\frac{1}{2N} \frac{\sigma_{\text{err}}^2}{\overline{F}^2}} \right)^2 + \left( \sqrt{\frac{\sigma_{\text{err}}^2}{N} \frac{1}{\overline{F}}} \right)^2 \right\}^{1/2}, \quad (3)$$

with  $S^2$ , the sample variance;  $\overline{\sigma_{\text{err}}^2}$ , the mean square error;  $\overline{F}$ , the mean flux.

In order to investigate the possible quasi-periodical behavior of the flux variations, we first constructed the Lomb-Scargle (LSP) periodogram (Lomb 1976; Scargle 1982), which is an improved Fourier-based technique suitable for the analysis of data with gaps.

polation for the data gaps (VanderPlas 2018):

$$P(f) = \frac{A^2}{2} \left( \sum_n g_n \cos(2\pi f[t_n - \tau]) \right)^2 + \frac{A^2}{2} \left( \sum_n g_n \sin(2\pi f[t_n - \tau]) \right)^2, \quad (4)$$

where  $A$ ,  $B$ , and  $\tau$  are arbitrary functions of the frequency  $f$  and observing times  $\{t_i\}$ . The LSP yields the most significant spectral power peak, and estimates its significance level by testing the false alarm probability of the null hypothesis.

Foster (1996) introduced the weighted wavelet Z-transform (WWZ) method, which is a periodicity analysis technique in both the time and frequency domains. Note that WWZ is suited for discovering variability timescales and is robust against missing data. It is defined as follows

$$WWZ = \frac{(N_{\text{eff}} - 3)V_y}{2(V_x - V_y)}, \quad (5)$$

with  $N_{\text{eff}}$ , the so-called effective number of data points;  $V_x$  and  $V_y$ , the weighted variation of the data  $x(t)$  and model function  $y(t)$ , respectively. WWZ is based on the Morlet wavelet (Grossmann & Morlet 1984)  $f(z) = e^{-cz^2}(e^{iz} - e^{-1/4c})$  where the constant  $e^{-1/4c}$  is inserted so that the wavelet's mean value is zero.

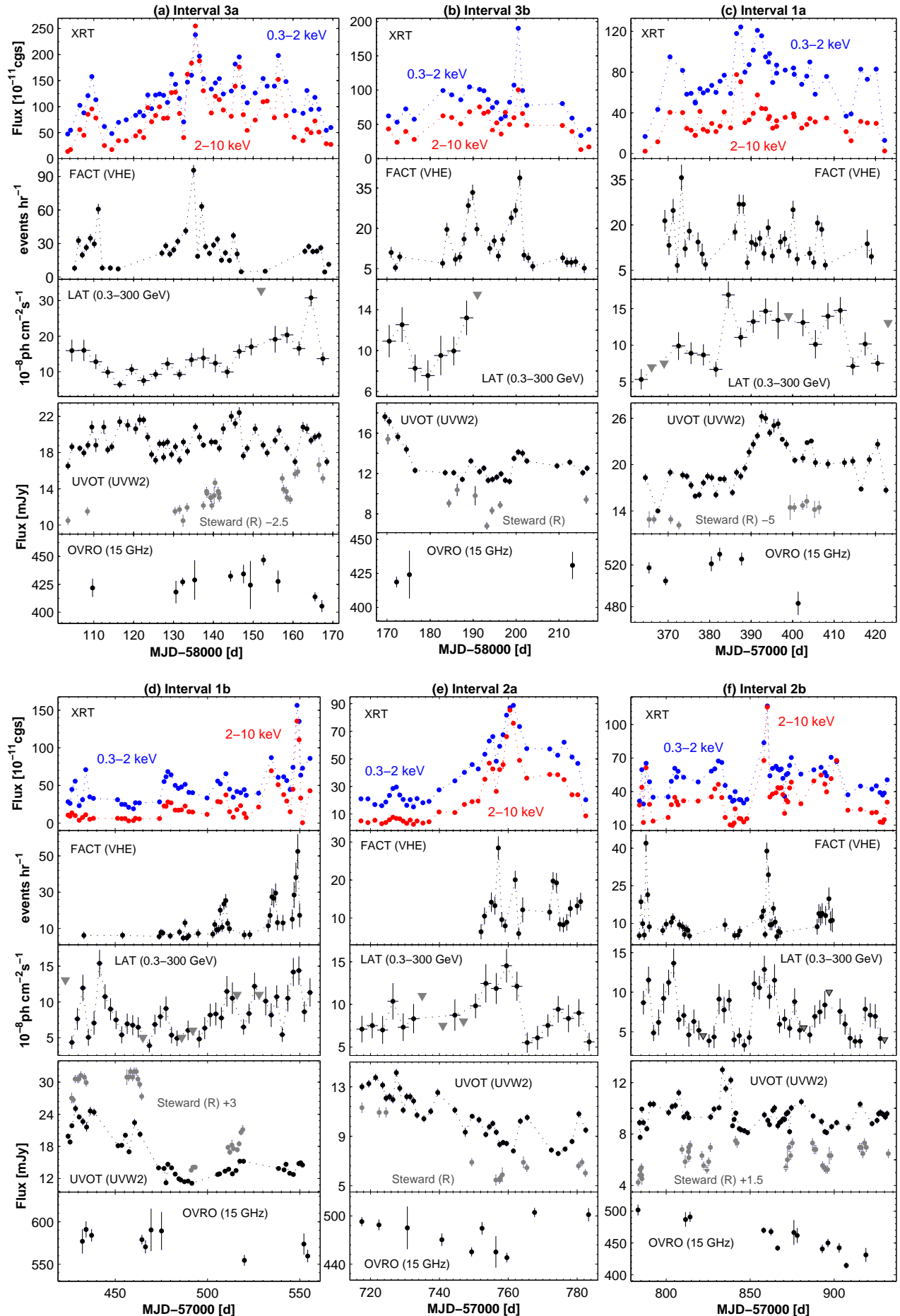
Throughout the paper, the errors are quoted at the 90% confidence level for the one parameter of interest, unless otherwise stated.

### 3. RESULTS

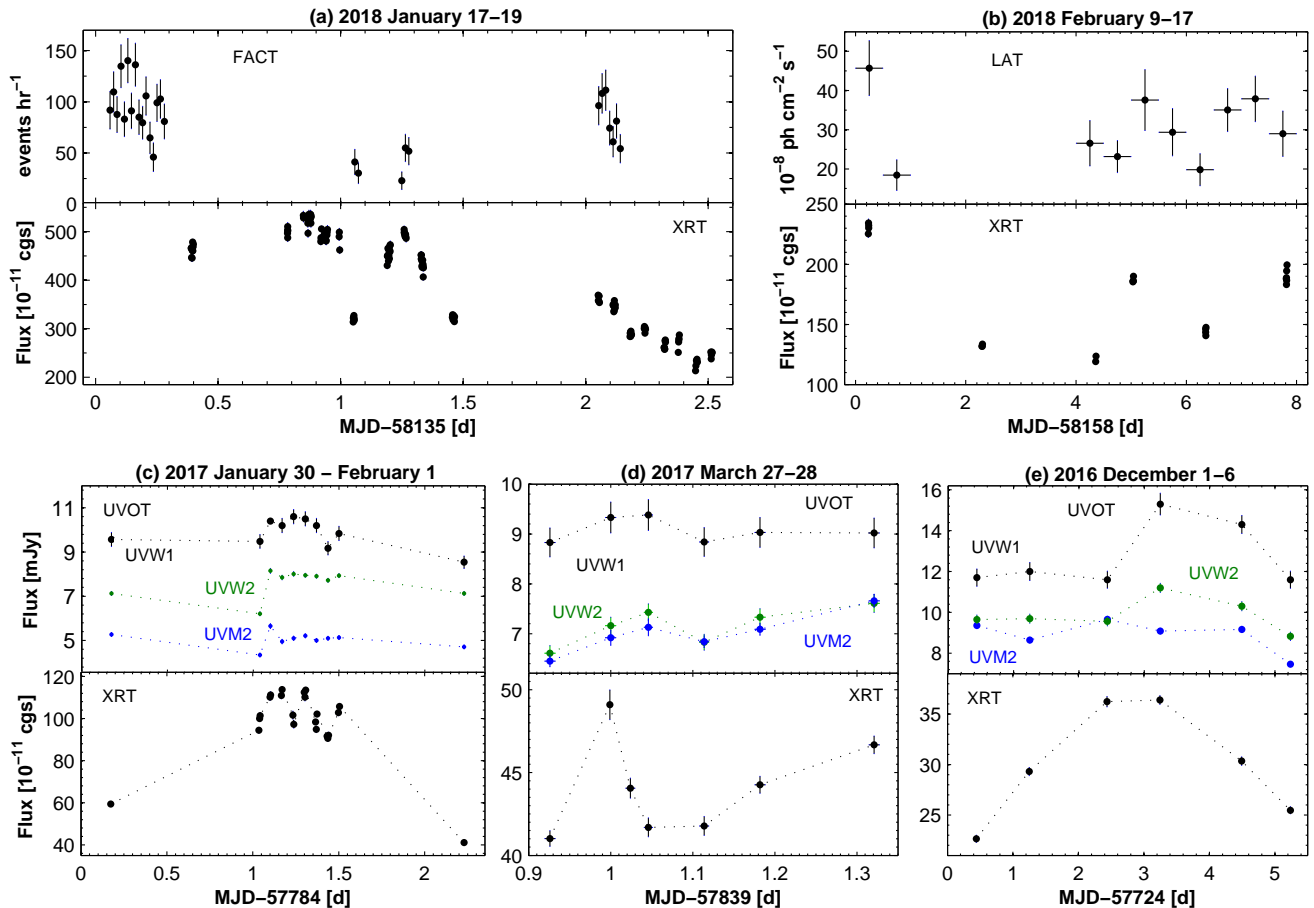
#### 3.1. X-Ray Variability

Table 2 provides a summary of the *Swift*-XRT and UVOT observations in 2015 December 8–2018 April 8. The source was targeted 299-times, with the net exposure time (sum of the Good Time Intervals, GTIs) of 314.5 ks. Based on the target's “visibility” for *Swift*, the observations were performed during 2015 December–2016 June, 2016 December–2017 June and 2017 December–2018 April, denoted as Interval 1, Interval 2, and Interval 3, respectively. For intervals 1 and 2, the observations were performed during 2015 December 8–2016 June 15, and for interval 3, during 2017 December 15–2018 April 8.





**Figure 6.** The MWL variability of Mrk 421 in different sub-intervals. The daily bins are used for the XRT, FACT, UVOT, Steward, OVRO light curves, while 3-d bins are used for the LAT 0.3–300 GeV data. The triangles in the LAT-related plots stand for the  $2\sigma$  upper limits to the 0.3–300 GeV flux when the source was detected below the  $5\sigma$  significance and/or showing  $N_{\text{pred}} < 10$ . The acronym



**Figure 7.** Intraday variability (IDV) of Mrk 421 in the FACT (panel (a)), LAT (panel (b)) and UVOT (panels (c)–(e)) bands.

split into two sub-periods (e.g., intervals 1a and 1b), according to the flaring activity of Mrk 421 in the *Swift*-XRT band.

The source was highly variable during all Intervals 1–3 (see Table 3 for the corresponding  $F_{\text{var}}$  and maximum-to-minimum flux ratios in different bands), although it showed significantly stronger X-ray flaring activity in Interval 3 compared to the previous ones (Figure 1a): the mean 0.3–10 keV count rate was a factor  $\sim 2$ –2.5 higher; during the eleven XRT pointings, the brightness exceeded a level of  $100 \text{ cts s}^{-1}$  (see Table 2), which never was recorded in Intervals 1–2; a generally higher state was superimposed by fast, strong flares by a factor of 2.2–3.8 (lasting 4–12 d) which were considerably fewer in the previous periods.

In Interval 3, the most extreme flare occurred during 2018 January 14–30 with a 2-min binned count rate of  $180.9 \pm 2.8 \text{ cts s}^{-1}$  (to the level observed on 2008 June 12; see Figure 1b) and the highest levels were recorded only during the giant X-ray outburst in 2013 April 10–17 (Kapanadze et al. 2016, 2018a). The source underwent fast brightness variations by 30%–45% within 13–35 ks during the declining phase of the flare (Figure 2, top panel). Note that the flux doubling time ( $\tau_d \approx 92 \text{ ks}$ , defined as  $\tau_d = \Delta t \times \ln(2) / \ln(F_2/F_1)$ ; Saito et al. 2013) was faster than the halving one ( $\tau_d \approx 113 \text{ ks}$ ), and a similar situation was seen during the next flare when an intraday flux doubling with  $\tau_d \approx 64 \text{ ks}$  was recorded (Figure 1b).

These events were preceded and followed by strong 0.3–10 keV flares by a factor of  $\sim 2.5$  and peak fluxes exceeding a level of  $100 \text{ cts s}^{-1}$  (Figures 1c–1c). They were parts of a well-defined long-term flare lasting more than 2 months (MJD 58103–58170). Other strong XRT-band flares are presented in Figures 1f–1i, with the intraday flux-doubling/halving events within 4.8–18.9 hr. Among

these flares, the 2015 December 29–2016 January 8 event was characterized by a two-peak maximum, possibly related to the propagation of forward and reverse shocks after the collision of two “blobs” in the blazar jet (see Böttcher & Dermer 2010).

The source also underwent extremely fast instances of the 0.3–10 keV intraday variability (IDV: brightness change within a day, detected by means of the chi-squared statistics; see Table 4 for details) at the 99.9% confidence level. Namely, the brightness showed a rise by 5%–18% (taking into account the associated measurement errors) in 180–600 seconds in Figures 3A1 (panels 1–2), 3C2–3C4, 3D3, 3E2 and 3E3–3E4. Figs 3A–3C belong to the epoch of the strongest X-ray flaring activity in 2018 January 14–30. Note that the states with  $\text{CR} \gtrsim 100 \text{ cts s}^{-1}$  sometimes were associated with very fast and large drops just at the start of the XRT orbit, which were related to instrumental effects. The source also showed very fast drops by 6–16 per cent within 180–840 seconds (Figures 3B1, 3C2, 3D1–3D3, 3F1–3F3). Finally, entire brightness rising and dropping cycles with 6%–13% within 420–960 seconds were also observed (Figures 3A2, 3B2, 3C1, 3E1). On the contrary, Mrk 421 sometimes showed a slow, low-amplitude variability during some densely-sampled XRT observations in lower X-ray states (see Figure 4). Moreover, tens of 0.3–10 keV IDVs were detected by us, whose details are reported in Table 4.

MAXI detected the source 78 and 61 times with  $5\sigma$  significance in the 2–20 keV and 2–6 keV energy ranges, respectively (Figure 5a–b). Owing to lower instrumental capabilities, a strong, long-term flare is evident only in Interval 3. Significantly fewer detections with  $5\sigma$  significance are found from the daily-binned BAT data, which show a strong flare during the highest XRT and MAXI-band states (Figure 5c).

**Table 5**

 The optical–UV and  $\gamma$ -ray IDVs during 2015 December–2018 April.

MJD (1)	Band (2)	$\Delta T$ (hr) (3)	$\chi^2/\text{dof}$ (4)	$100 \times F_{\text{var}}$ (5)
57380.79–57381.56	<i>UVW2</i>	17.47	12.46/1	8.5(1.8)
57391.56–57392.21	<i>UVW1</i>	12.26	7.77/2	10.3(2.3)
57425.25–57426.23	<i>UVM2</i>	22.37	23.24/1	7.2(1.1)
57426.18–57426.49	<i>UVW2</i>	6.38	12.38/1	8.0(1.7)
57430.17–57430.35	<i>UVM2</i>	3.29	14.88/1	4.6(0.9)
57477.97–57478.21	<i>UVM2</i>	4.61	14.67/1	7.0(1.4)
57477.97–57478.21	<i>UVW2</i>	4.58	49.42/1	18.5(1.9)
57724.44–57725.29	<i>UVM2</i>	19.39	12.31/1	5.4(1.2)
57726.44–57727.29	<i>UVW1</i>	19.44	29.94/1	19.1(2.5)
57726.44–57727.29	<i>UVW2</i>	19.44	27.79/1	11.0(1.5)
57728.49–57729.28	<i>UVW1</i>	17.88	19.70/1	14.4(2.4)
57728.49–57729.28	<i>UVM2</i>	17.98	78.32/1	14.4(1.2)
57728.49–57729.28	<i>UVW2</i>	17.81	24.44/1	10.6(1.6)
57755.22–57756.20	<i>UVM2</i>	22.32	22.63/1	9.0(1.4)
57784.17–57785.08	<i>UVM2</i>	20.66	53.39/1	13.6(1.3)
57784.17–57785.08	<i>UVW2</i>	20.69	16.47/1	9.5(1.7)
57785.03–57785.54	<i>UVW1</i>	11.14	4.17/7	4.1(1.2)
57785.03–57785.54	<i>UVM2</i>	11.12	13.94/7	6.9(0.7)
57785.03–57785.54	<i>UVW2</i>	11.11	15.95/7	7.7(0.8)
57785.37–57786.27	<i>UVW1</i>	20.76	6.04/3	7.1(1.7)
57785.37–57786.27	<i>UVM2</i>	20.74	5.56/1	3.5(0.9)
57785.37–57786.27	<i>UVW2</i>	20.72	5.67/1	4.4(1.1)
57839.93–57840.37	<i>UVM2</i>	9.50	10.74/5	5.3(0.8)
57839.93–57840.37	<i>UVW2</i>	9.53	6.48/5	5.3(0.9)
57843.91–57844.41	<i>UVM2</i>	9.51	21.80/1	8.3(1.3)
57873.87–57874.12	<i>UVM2</i>	4.85	12.68/1	6.1(1.3)
57873.87–57874.12	<i>UVW2</i>	4.86	40.44/1	14.3(1.6)
57926.42–57927.40	<i>UVM2</i>	22.27	14.22/1	6.19(1.2)
58103.44–58104.34	<i>UVM2</i>	20.66	28.82/1	8.9(1.2)
58103.44–58104.34	<i>UVW2</i>	20.64	12.50/1	7.8(1.6)
58112.36–58113.35	<i>UVM2</i>	8.28	38.20/1	13.3(1.5)
58123.91–58124.48	<i>UVM2</i>	12.65	26.45/1	9.3(1.3)
58123.91–58124.48	<i>UVW2</i>	12.64	12.46/1	7.7(1.6)
58137.05–58137.55	<i>UVW1</i>	11.05	13.41/1	11.7(2.4)
58146.68–58147.32	<i>UVW1</i>	14.50	29.12/1	18.2(2.4)
58146.68–58147.32	<i>UVW2</i>	14.49	46.25/1	16.2(1.7)
58147.217–58148.12	<i>UVM2</i>	19.03	14.88/1	6.2(1.2)
58199.81–58200.06	<i>UVW1</i>	4.73	19.56/1	13.5(2.2)
58139.60–58140.40	<i>V</i>	19.20	14.19/2	7.2(1.7)
58139.60–58140.40	<i>R</i>	19.21	7.59/2	7.2(2.2)
58158.00–58158.98	0.3–300 GeV	23.52	11.62/1	57.6(12.8)
58135.059–58136.058	VHE	23.58	2.82/16	23.4(5.4)
58135.236–58136.073	VHE	20.09	4.44/5	41.1(10.1)
58136.250–58137.141	VHE	21.38	4.22/9	32.3(7.8)

### 3.2. Multiwavelength Variability on Various Timescales

Similar to the XRT-band, the strongest FACT VHE  $\gamma$ -ray flaring activity of Mrk 421 occurred in Period 3a (Figure 6a). Namely, two strong flares peaking at MJD 58111 and MJD 58135, as well as lower-amplitude ones with the peaks at MJD 58141, 58145 and 58164 accompanied the X-ray counterparts. The UVOT-band behaviour was also predominantly correlated with the 0.3–10 keV flaring activity, while the source demonstrated different timing properties in the LAT-band, showing slower variability and only one peak at the end of this sub-interval, coinciding with the X-ray and VHE peaks.

The three subsequent peaks in the FACT-band light curve were evident during the strongest 0.3–10 keV activity of the source in Interval 3b (Figure 6b). No LAT-band GTIs were obtained during the second half of this period and a correlated behaviour with X-ray variability was not observed in the first half. The optical–UV light curves showed a decline at the beginning of the sub-interval, followed by the weak variability which was not strongly correlated with the VHE–X-ray activity. However, a stronger correlation was observed during Period 1a, in the three consecutive peaks having X-ray and VHE counterparts (Figure 6c). Similarly, the LAT-band behaviour

was more correlated with those in the XRT and FACT bands, compared to that shown in Interval 3.

The majority of Interval 1b also was characterized by a correlated X-ray and VHE flaring activity (Figure 6d). The peak days of the X-ray–VHE fluxes also coincided with enhanced activity of Mrk 421 in the LAT-band. However, the source was not targeted with *Swift* and FACT during the strongest GeV-band flare peaking on MJD 57441. Initially, the source was flaring at UV-optical frequencies (correlated with the higher-energy activity), while it showed a declining trend and low states afterwards, during the four consecutive keV–TeV flares. A similar situation was observed in Interval 2a when the source exhibited enhanced VHE and LAT-band activities during the long-term X-ray flare (see Figure 6e). Finally, Mrk 421 underwent strong VHE flares along with the X-ray ones in Interval 2b, while the latter showed fewer correlation with the LAT and UVOT-band fluctuations (Figure 6f). The source did not show flares at the radio frequencies during any sub-interval (see the bottom panels of Figure 6).

Although Mrk 421 frequently showed 8–16 detections a night with  $3\sigma$  significance in the 20-min binned FACT data (particularly, in the time interval 2018 January–February), only 3 instances of a VHE IDV at the 99.9% confidence level were detected<sup>18</sup>, belonging to the epoch of the strongest X-ray flaring activity in the period presented here (see Figure 7a and Table 5). While no correlated X-ray–VHE variability was evident during MJD 58136.1–58136.3, the subsequent VHE data exhibit a brightness decline similar to the XRT ones. In the same period, the source showed one instance of a LAT-band IDV with a brightness decline by 42% (taking into account the associated errors) and accompanied by similar behaviour in X-rays (Figure 7b). Finally, three ultraviolet IDVs, showing a brightness increase nearly simultaneously with that in the 0.3–10 keV energy range, are presented in Figures 7c–7d. The details of another 35 optical–UV IDVs are provided in Table 5.

### 3.3. Spectral Variability

#### 3.3.1. Curvature Parameter

Similar to the period 2005 March–2015 June (Kapanadze et al. 2016, 2017a, 2018a,b), a vast majority of the 0.3–10 keV spectra of Mrk 421 (886 out of 980) show a significant curvature and are well fitted with the log-parabolic model. The corresponding results are presented in Table 6. The distribution of values of the curvature parameter  $b$  (corresponding to the curvature detection significance of  $3\sigma$  and higher) for different periods are provided in Figures 8A1–8A4 and the corresponding properties (minimum, maximum and mean values, distribution skewness) are listed in Table 7.

Figure 8A1 demonstrates that the source was characterized by a relatively low curvature in the period 2015 December–2018 April: 98.1% of the values of the parameter  $b$  were smaller than  $b=0.4$  (conventional threshold between the lower and higher curvatures). Moreover, 46.2% of the spectra shows  $b<0.2$  (see Section 4.3 for the corresponding physical implication). The lowest curvatures were observed in Interval 3: there were no spectra with  $b>0.4$ ; 62.3% of the values were lower than 0.2; the mean value  $\bar{b}=0.18\pm 0.01$  is significantly smaller than that recorded in Interval 1 (see Table 7). The latter was characterized by the majority of the spectra showing curvatures with  $b>0.4$  (5 out of 9, including the highest value

<sup>18</sup> Note that the FACT results are still provided in the form of the excess rates, and this result should be considered with caution.

**Table 6**

The results of the *Swift*-XRT spectral analysis with the log-parabolic model (extract; see the corresponding machine-readable table for the full version). Col. (1) gives the ObsID of the particular observation, along with the duration of the separate segments (in seconds) used to extract a spectrum in parentheses. The abbreviations “Or” and “S” stand for “orbit” and “segment”, respectively; Cols (2)–(3) present the values of the photon index at 1 keV and the curvature parameter, respectively. The  $E_p$  values (Col. (4)) are given in keV; Cols 5 and 6 present the norm and the reduced Chi-squared, respectively; de-absorbed 0.3–2 keV, 2–10 keV and 0.3–10 keV fluxes (Col. (7)–(9)) - in  $\text{erg cm}^{-2}\text{s}^{-1}$ . The hardness ratio is presented in the last column.

ObsId	$a$	$b$	$E_p$	$10 \times K$	$\chi^2/d.o.f.$	$F_{0.3-2\text{ keV}}$	$F_{2-10\text{ keV}}$	$F_{0.3-10\text{ keV}}$	HR
(1)	(2)	(3)	(4)	(5)	(6)	(7)	(8)	(9)	(10)
35014240	2.92(0.02)	0.27(0.08)	0.02(0.01)	0.41(0.01)	1.04/145	16.71(0.27)	2.34(0.14)	19.05(0.35)	0.14(0.01)
35014241	2.49(0.01)	0.48(0.04)	0.31(0.05)	1.31(0.01)	1.10/244	43.35(0.40)	11.59(0.32)	54.95(0.50)	0.27(0.01)
35014242 S1 (267 s)	2.22(0.02)	0.38(0.04)	0.51(0.06)	3.12(0.04)	1.07/230	94.62(1.08)	40.46(1.19)	135.21(1.55)	0.43(0.01)
35014242 S2 (267 s)	2.24(0.02)	0.40(0.04)	0.50(0.06)	3.19(0.04)	1.00/236	97.05(1.11)	39.90(1.18)	136.77(1.57)	0.41(0.01)

**Table 7**

Distribution of spectral parameters in different periods: minimum and maximum values (Cols (2) and (3), respectively), mean value (Col. (4)) and skewness (last column).

Par.	Min.	Max.	Mean	Skewness
(1)	(2)	(3)	(4)	(5)
2015–2018				
$b$	0.07(0.04)	0.48(0.04)	0.20(0.01)	0.66
$a$	1.63(0.02)	2.92(0.02)	2.12(0.01)	0.58
$\Gamma$	1.79(0.02)	2.91(0.02)	2.12(0.02)	0.98
HR	0.14(0.01)	1.23(0.03)	0.64(0.01)	0.28
$E_p$	0.50(0.06)	7.50(0.76)	1.85(0.09)	1.65
Int1				
$b$	0.07(0.04)	0.48(0.04)	0.25(0.01)	0.34
$a$	1.77(0.02)	2.92(0.02)	2.29(0.01)	0.31
$\Gamma$	1.99(0.02)	2.91(0.02)	2.12(0.04)	1.37
HR	0.14(0.01)	0.89(0.03)	0.45(0.01)	0.91
$E_p$	0.50(0.06)	2.03(0.14)	1.02(0.18)	0.94
Int1a				
$b$	0.09(0.04)	0.48(0.04)	0.25(0.01)	0.61
$a$	1.98(0.02)	2.92(0.02)	2.30(0.01)	-0.37
HR	0.14(0.01)	0.68(0.02)	0.42(0.01)	0.98
Int1b				
$b$	0.08(0.04)	0.42(0.05)	0.25(0.01)	0.25
$a$	1.77(0.02)	2.91(0.02)	2.26(0.01)	0.41
HR	0.14(0.01)	0.89(0.03)	0.49(0.01)	0.33
Int2				
$b$	0.07(0.04)	0.42(0.05)	0.20(0.01)	0.58
$a$	1.74(0.02)	2.82(0.02)	2.12(0.01)	1.02
$\Gamma$	1.92(0.02)	2.54(0.02)	2.13(0.03)	1.22
HR	0.17(0.01)	1.09(0.03)	0.63(0.01)	-0.20
$E_p$	0.51(0.06)	6.31(0.65)	1.46(0.22)	2.17
Int2a				
$b$	0.10(0.04)	0.40(0.04)	0.22(0.01)	0.48
$a$	1.74(0.02)	2.82(0.02)	2.14(0.01)	0.84
HR	0.17(0.01)	1.09(0.03)	0.61(0.01)	-0.23
Int2b				
$b$	0.07(0.04)	0.40(0.04)	0.18(0.01)	0.12
$a$	1.80(0.02)	2.50(0.02)	2.10(0.01)	0.47
HR	0.29(0.01)	1.06(0.04)	0.65(0.01)	0.14
Int3				
$b$	0.07(0.04)	0.36(0.04)	0.18(0.01)	0.53
$a$	1.63(0.02)	2.64(0.01)	2.01(0.01)	0.43
$\Gamma$	1.79(0.02)	2.60(0.02)	2.08(0.02)	0.05
HR	0.28(0.01)	1.23(0.03)	0.75(0.01)	0.19
$E_p$	0.50	7.50(0.76)	2.16(0.17)	1.30
Int3a				
$b$	0.07(0.04)	0.30(0.04)	0.17(0.01)	0.34
$a$	1.63(0.02)	2.52(0.02)	1.98(0.01)	0.54
HR	0.28(0.01)	1.23(0.03)	0.79(0.01)	-0.04
Int3b				
$b$	0.08(0.04)	0.36(0.04)	0.21(0.01)	0.16
$a$	1.95(0.02)	2.39(0.02)	2.11(0.01)	0.78
HR	0.36(0.02)	0.80(0.03)	0.60(0.01)	-0.19

for the entire 2.3-yr period presented here). Interval 2 was different from both cases and characterized by “intermediate” properties of the parameter  $b$  between Intervals 1 and 3. This situation is clearly evident from the cumulative distributions of the curvature parameter pre-

of the K-S test and distances between the corresponding distributions.

According to Figure 8A3 and Table 8, the distribution of the parameter  $b$  shows differences between the different parts of Intervals 2–3. The lowest curvatures are found for Interval 3a ( $\bar{b}=0.17\pm 0.01$ , 66% of the spectra with  $b<0.2$ , and  $b_{\text{max}}0.30\pm 0.04$ ), while Intervals 1a and 1b are not significantly different from each other.

The curvature parameter showed a weak positive correlation with the photon index at 1 keV and an anti-correlation with the position of the synchrotron SED peak, as observed in different sub-intervals (see Figures 9a–9b, as well as Table 9 for the corresponding values of the Spearman correlation coefficient  $\rho$ ). Moreover, this parameter showed an anti-correlation with the de-absorbed 0.3–10 keV flux in Intervals 1–2 (Figure 9c).

The sixth column of Table 4 demonstrates that the parameter  $b$  was variable 36-times at the  $3\sigma$  confidence level during 0.3–10 keV IDVs, showing  $\Delta b=0.14(0.05)$ – $0.31(0.06)$  within 0.38–23.92 hr (Figures 2–4). The fastest instances incorporated a curvature increase by 0.19(0.06)–0.22(0.06) in  $\sim 1$  ks (Figure 2, at MJD 58135.93; Figure 4, at MJD 57375.4). Moreover, the curvature parameter varied with  $2\sigma$  and  $1\sigma$  significances (capable of causing a significant flux change) 43 and 22 times, respectively.

### 3.3.2. Photon Index and Hardness Ratio

Although the photon index at 1 keV showed a very wide range of values ( $\Delta a=1.29$ ) with the hardest spectrum yielding  $a=1.63\pm 0.02$  in the period presented here, this range is narrower compared to that recorded in the time interval 2009–2012 ( $\Delta a=1.51$ ). In the latter, the source showed the hardest ( $a=1.51$ – $1.61$ ) and the softest spectra ( $a=2.93$ – $3.02$ ) since the start of the *Swift* operations. On the other hand, narrower ranges were found in the time intervals 2005–2008, 2013 April and 2013 November–2015 June (1.01, 0.87 and 0.94, respectively).

Similar to the previous periods, the source clearly demonstrated a “harder-when-brighter” spectral behaviour during the 0.3–10 keV flares. Figure 9d exhibits a strong anti-correlation between the parameter  $a$  and the de-absorbed 0.3–10 keV flux (see also Table 9). This trend was evident in Intervals 1–3 and sub-intervals separately, although with different strengths and slopes of the corresponding scatter plot. Moreover, Figure 10b shows some short time intervals when the opposite spectral trend was observed (during MJD 57370.42–57374.47, 57426.45–57428.31 etc.).

294 spectra were harder than  $a=2$  (conventional threshold between the hard and soft X-ray spectra), amounting to 33.2% of all log-parabolic spectra (see Figure 8B1). Note that this percentage is smaller than in the periods 2005–2008, 2009–2012, 2013 January–May (39%–46%) and higher than those shown in 2013 November–2015 June (29%).

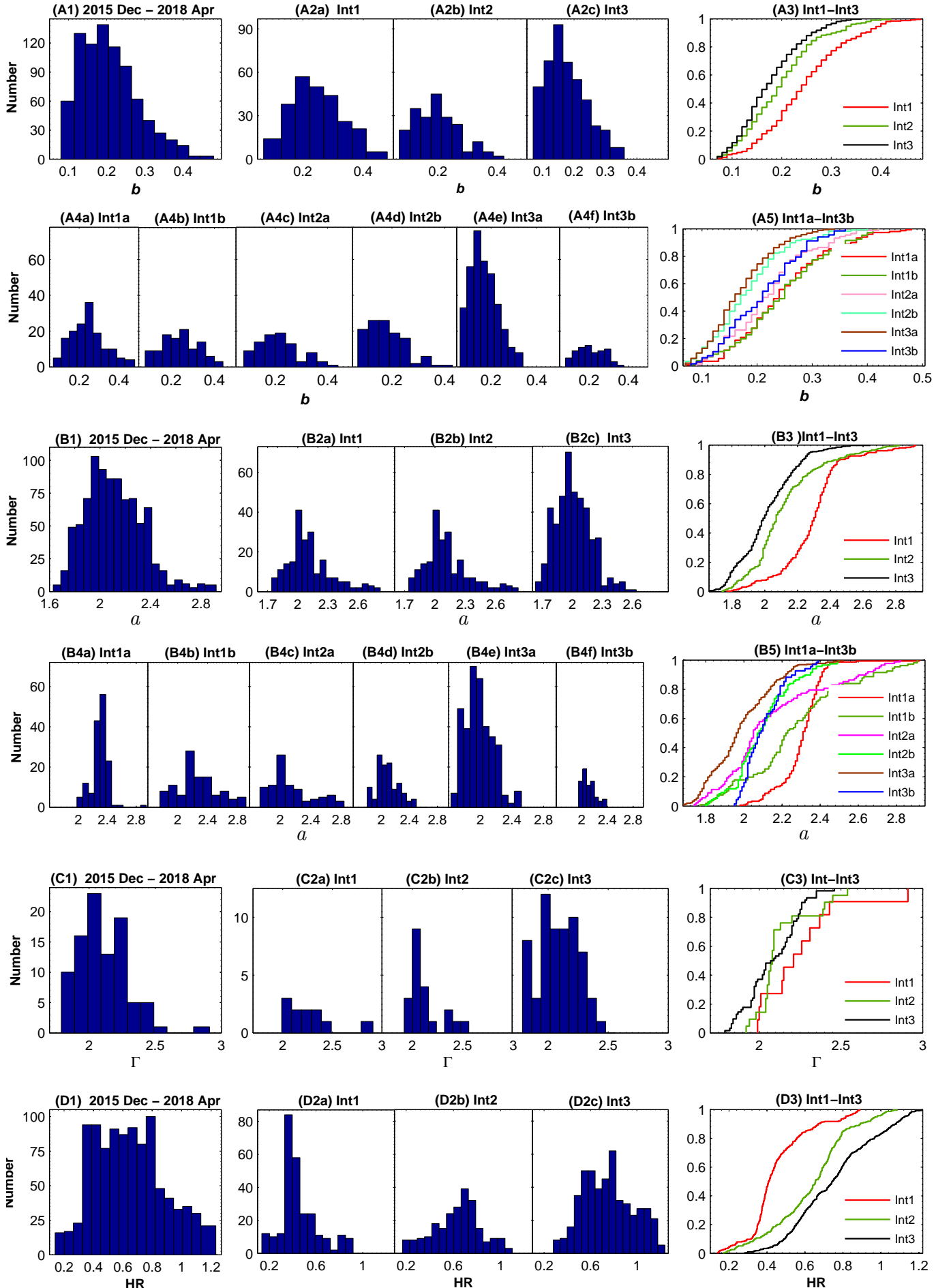


**Figure 8.** Distribution of the spectral parameter values in different periods: histograms and the corresponding normalized cumulative distributions (the last plot in each row).

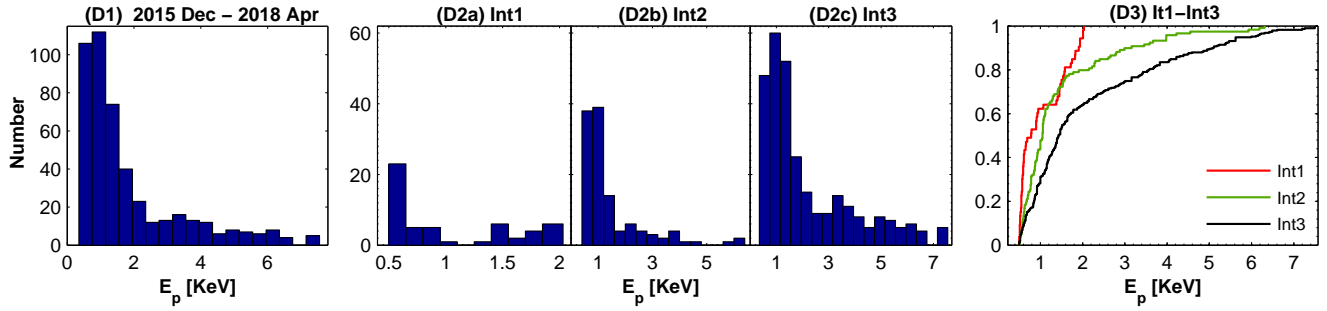
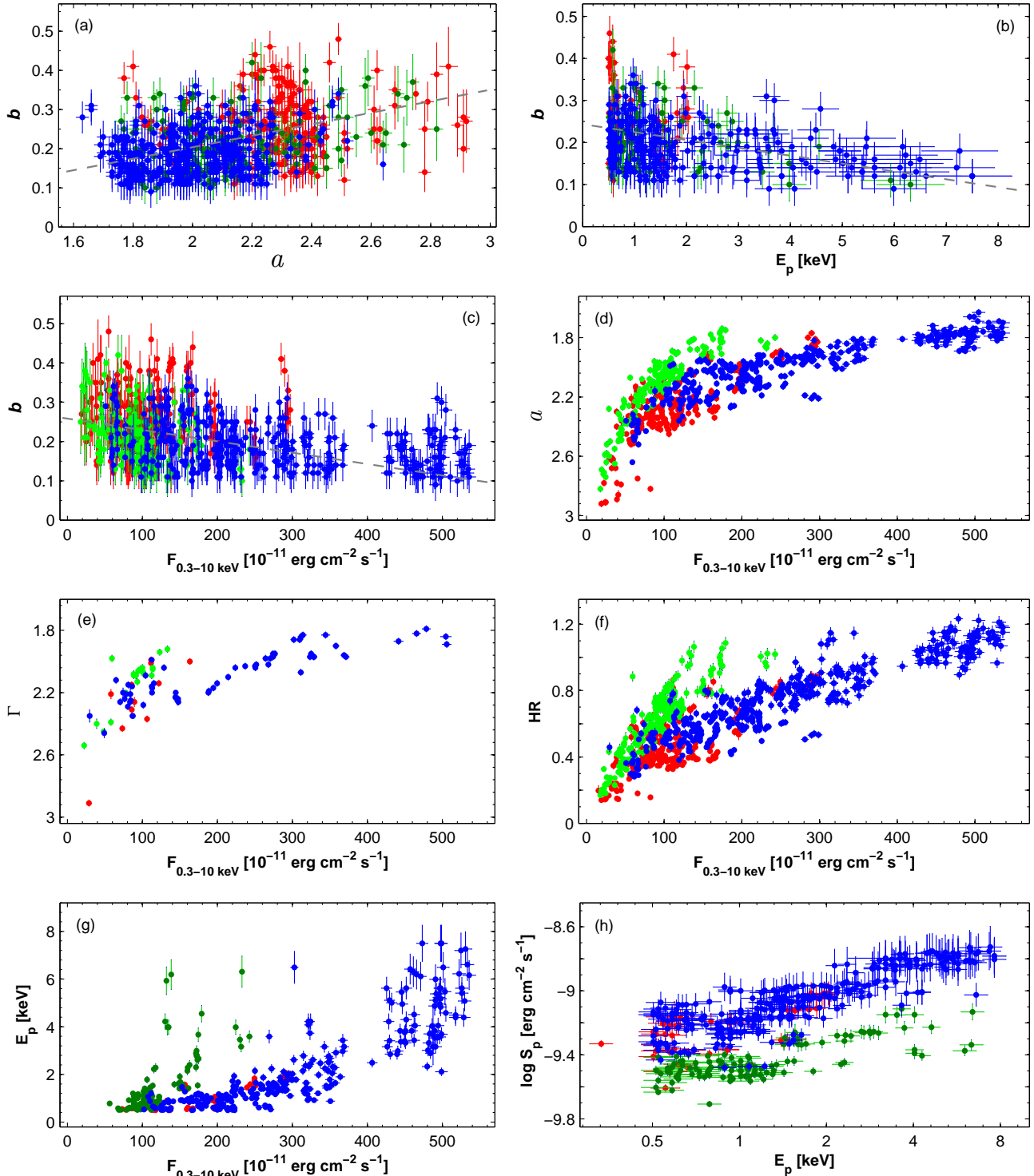


Figure 8. - Continued.



**Figure 9.** Correlation between the spectral parameters and de-absorbed 0.3–10 keV flux. Panels (a)–(3): the curvature parameter  $b$  plotted versus the photon index  $a$ , the position of the synchrotron SED peak  $E_p$  and de-absorbed 0.3–10 keV flux, respectively. The parameters  $a$ ,  $\Gamma$ , HR and  $E_p$  are plotted versus the de-absorbed 0.3–10 keV flux in Panels (d)–(g). The scatter plot  $E_p$ – $\log S_p$  is provided in the last plot. The colored linear points correspond to the different intervals as follows: red – Interval 1; green – Interval 2; blue – Interval 3. Gray dashed lines represent linear fits to the scatter plots.

**Table 8**

Results from the KS-test. In Cols (2)–(7), the symbol “1” indicates that data sets are different from each other, and the corresponding distance between the normalized cumulative distributions are provided in Cols (8)–(13); “0”- no significant difference between the data sets.

Quant.	KS						$D_{KS}$					
	Int1–Int2	Int1–Int3	Int2–Int3	Int1a–Int1b	Int2a–Int2b	Int3a–Int3b	Int1–Int2	Int1–Int3	Int2–Int3	Int1a–Int1b	Int2a–Int2b	Int3a–Int3b
(1)	(2)	(3)	(4)	(5)	(6)	(7)	(8)	(9)	(10)	(11)	(12)	(13)
$b$	1	1	1	0	1	1	0.25	0.38	0.15	-	0.34	0.27
$a$	1	1	1	1	1	1	0.49	0.61	0.26	0.32	0.19	0.47
$\Gamma$	0	0	0	-	-	-	-	-	-	-	-	-
HR	1	1	1	1	0	1	0.50	0.62	0.25	0.31	-	0.55
$E_p$	0	1	1	-	-	-	-	0.37	0.28	-	-	-

**Table 9**

Correlations between spectral parameters and 0.3–10 keV flux in different periods. In Cols (2)–(3),  $\rho$  and  $p$  stand for the Spearman coefficient and the corresponding p-chance, respectively.

Quantities	$\rho$	$p$
2015 Dec–2018 Apr		
$a$ and $b$	0.33(0.08)	$6.23 \times 10^{-6}$
$b$ and $E_p$	-0.34(0.09)	$1.04 \times 10^{-6}$
$b$ and $F_{0.3-10 \text{ keV}}$	-0.33(0.10)	$3.42 \times 10^{-6}$
$a$ and $F_{0.3-10 \text{ keV}}$	-0.80(0.03)	$3.08 \times 10^{-14}$
$\Gamma$ and $F_{0.3-10 \text{ keV}}$	-0.75(0.07)	$7.42 \times 10^{-13}$
HR and $F_{0.3-10 \text{ keV}}$	0.79(0.04)	$4.19 \times 10^{-14}$
$E_p$ and $F_{0.3-10 \text{ keV}}$	0.69(0.08)	$4.34 \times 10^{-12}$
$\log E_p$ and $\log S_p$	0.65(0.08)	$3.39 \times 10^{-11}$
$\Gamma_{0.3-2 \text{ GeV}}$ and $\Gamma_{2-300 \text{ GeV}}$	0.39(0.09)	$1.99 \times 10^{-8}$
Int1		
$a$ and $b$	0.29(0.09)	$1.00 \times 10^{-5}$
$a$ and $F_{0.3-10 \text{ keV}}$	-0.70(0.04)	$6.56 \times 10^{-12}$
$\Gamma$ and $F_{0.3-10 \text{ keV}}$	-0.73(0.907)	$3.04 \times 10^{-6}$
HR and $F_{0.3-10 \text{ keV}}$	0.64(0.06)	$1.24 \times 10^{-10}$
$E_p$ and $F_{0.3-10 \text{ keV}}$	0.73(0.08)	$2.51 \times 10^{-10}$
$\log E_p$ and $\log S_p$	0.64(0.07)	$8.99 \times 10^{-10}$
Int2		
$a$ and $b$	0.23(0.08)	$3.34 \times 10^{-4}$
$b$ and $E_p$	-0.30(0.10)	$8.60 \times 10^{-5}$
$b$ and $F_{0.3-10 \text{ keV}}$	-0.31(0.10)	$9.11 \times 10^{-6}$
$a$ and $F_{0.3-10 \text{ keV}}$	-0.88(0.03)	$< 10^{-15}$
$\Gamma$ and $F_{0.3-10 \text{ keV}}$	-0.70(0.10)	$7.66 \times 10^{-5}$
HR and $F_{0.3-10 \text{ keV}}$	0.88(0.03)	$< 10^{-15}$
$E_p$ and $F_{0.3-10 \text{ keV}}$	0.69(0.09)	$7.15 \times 10^{-9}$
$\log E_p$ and $\log S_p$	0.62(0.07)	$6.02 \times 10^{-10}$
Int3		
$a$ and $b$	0.32(0.08)	$6.23 \times 10^{-12}$
$b$ and $E_p$	-0.32(0.09)	$4.48 \times 10^{-5}$
$b$ and $F_{0.3-10 \text{ keV}}$	-0.30(0.11)	$8.19 \times 10^{-5}$
$a$ and $F_{0.3-10 \text{ keV}}$	-0.86(0.03)	$1.03 \times 10^{-15}$
$\Gamma$ and $F_{0.3-10 \text{ keV}}$	-0.85(0.05)	$2.47 \times 10^{-14}$
HR and $F_{0.3-10 \text{ keV}}$	0.89(0.03)	$< 10^{-15}$
$E_p$ and $F_{0.3-10 \text{ keV}}$	0.85(0.06)	$1.69 \times 10^{-14}$
$\log E_p$ and $\log S_p$	0.83(0.05)	$5.54 \times 10^{-14}$

2018a,b). On average, the hardest spectra with the mean value  $\bar{a}=1.98 \pm 0.01$  were observed in Interval 3a versus the softest spectra belonging to Interval 1 ( $\bar{a}=2.29 \pm 0.01$ ). Figures 8B2–8B5 and Table 8 clearly show that the distribution properties of the parameter  $a$  varied not only from interval to interval, but also among the sub-intervals.

Similar to the curvature parameter  $b$ , the photon index  $a$  showed an extreme variability on diverse timescales. It varied at the  $3\sigma$  confidence level 69 times with  $\Delta a=0.08(0.03)$ – $0.31(0.02)$  within 0.27–23.97 hr along with the X-ray IDVs (see Col. (5) of Table 4 and Figures 2–4). Among them, 5 subhour instances were recorded: hardenings by  $\Delta a=0.08(0.03)$ – $0.23(0.03)$  within 0.13–0.28 hr. On longer timescales, the largest variabilities with  $\Delta a=0.66$ – $1.07$  in 3.1–27.6 d were observed along with the strong 0.3–10 keV flares (Figure 10b).

The hardness ratios, derived from the log-parabolic and power-law spectra, showed a wide range of values ( $A_{HR} = 1.00$ ) with 69.7% of all spectra with  $HR > 0.5$

and 90 spectra (9.2%) showing  $HR > 1$  (see Figure 8D1 and Table 7) when the de-absorbed 2–10 keV flux is higher than the 0.3–2 keV one. A vast majority of the latter (90%) belong to Interval 3a, characterized by the highest mean value  $\overline{HR}=0.79 \pm 0.01$  (versus  $\overline{HR}=0.42$ – $0.65$  in other sub-intervals; Figures 8D2–8D3). A positive  $F_{0.3-10 \text{ keV}}$ –HR correlation was observed in all intervals, demonstrating a dominance of the “harder-when-brighter” spectral evolution during X-ray flares, although this trend was significantly weaker in Interval 1 (see Figure 9f) and Table 9). The long-term behaviour of the hardness ratio followed that of the parameter  $a$ : during the largest variability of the photon index, HR increased by a factor of 3.5–6.4 and showed 75 IDVs by 11%–88% per cent (see Col. (8) of Table 4).

### 3.3.3. The Position of the Synchrotron SED Peak

During the period 2015 December–2018 April, 463 spectra (52.3% of those showing a curvature) are characterized by  $0.5 \leq E_p \leq 8$  keV when the position of the synchrotron SED peak is well-constrained by the XRT data (see Kapanadze et al. 2018b). In the case of 407 spectra (46%),  $E_p < 0.5$  keV when the synchrotron SED peak position, derived via the X-ray spectral analysis, should be assumed as an upper limit to the intrinsic peak position (not used by us for the construction of the scatter plots and distributions). Note that such instances amounted to 86.6% and 68.9% of all curved spectra from Intervals 1a and 1b, respectively (versus 25.4% in Interval 3a). Moreover, the majority of the spectra with  $E_p < 0.1$  keV (when the synchrotron SED peak is situated in the UV energy range) belonged to these sub-intervals.

On the other hand, for the spectra with  $E_p > 8$  keV, the synchrotron SED peak is poorly constrained by the observational data and such  $E_p$  values should be considered as lower limits to the intrinsic position (see Kapanadze et al. 2018b). During the period 2018 December–2018 April, the source showed 14 spectra with  $8.25 \leq E_p \leq 15.85$  keV, mostly from the observations corresponding to the highest X-ray states in Interval 3a.

The  $E_p$  values from the range 0.5–8 keV mainly belong to Interval 3 (62.9%), and their mean is significantly higher than those from Intervals 1–2 (2.16 keV versus 1.02–1.46 keV in Intervals 1–2; see Figures 8D2 and Table 7). Note that the K-S test and related Monte Carlo simulations did not show a significant difference between the distributions corresponding to Intervals 1 and 2 (see Table 8). For the entire 2015 December–2018 April period, the parameter  $E_p$  showed a positive correlation with  $F_{0.3-10 \text{ keV}}$ , which was the strongest in Interval 3 (Figure 9g and Table 9). Moreover, a positive correlation between  $E_p$  and  $S_p$  (the height of the synchrotron SED peak) was detected in all three time intervals (see Figure 9h, Table 9 and Section 4.3 for the corresponding physical implication). Note that the latter quantity was calculated for each spectrum as (Massaro et al. 2004)

$$S_p = 1.6 \times 10^{-9} K 10^{(2-a)/4b} \text{ erg cm}^{-2} \text{ s}^{-1}. \quad (6)$$

**Table 10**

The results of the XRT spectral analysis with a simple power-law model (extract; see the corresponding machine-readable table for the full version). Col. (1) gives the ObsID of the particular observation, along with the duration of the separate segments (in seconds) used to extract a spectrum in parentheses. The acronyms ‘‘Or’’ and ‘‘S’’ stand for ‘‘orbit’’ and ‘‘segment’’, respectively. The value of the 0.3–10 keV photon index is provided in Col. (2); Cols (3) and (4) present the norm and the reduced Chi-squared, respectively; de-absorbed 0.3–2 keV, 2–10 keV and 0.3–10 keV fluxes (Cols (5)–(7)) are given in  $\text{erg cm}^{-2} \text{s}^{-1}$ . The hardness ratio is presented in the last column

ObsId (1)	$\Gamma$ (2)	$10 \times K$ (3)	$\chi^2/d.o.f.$ (4)	$F_{0.3-2 \text{ keV}}$ (5)	$F_{2-10 \text{ keV}}$ (6)	$F_{0.3-10 \text{ keV}}$ (7)	HR (8)
35014245 Or5	2.31(0.02)	1.73(0.02)	0.95/186	57.68(0.66)	28.12(0.83)	85.90(1.18)	0.49(0.02)
35014246 Or4	2.43(0.02)	1.51(0.02)	0.88/182	52.60(0.60)	20.70(0.52)	73.28(0.67)	0.39(0.01)
34228001 Or1 S2 (410 s)	2.15(0.02)	1.64(0.02)	1.09/229	51.88(0.71)	33.81(0.77)	85.70(0.98)	0.65(0.02)
34228001 Or2 S2 (285 s)	2.14(0.02)	2.32(0.02)	1.08/233	73.45(0.84)	48.42(1.10)	121.90(1.40)	0.66(0.02)
34228023	2.26(0.03)	1.77(0.03)	0.91/139	58.34(1.06)	31.05(1.26)	89.33(1.43)	0.53(0.02)

On intraday timescales, the parameter  $E_p$  varied 56 times at the 3 $\sigma$  confidence level, observed during the 0.3–10 keV IDVs (see Col. (7) of Table 4). The most dramatic changes were observed during the extreme flare in 2018 January 14–30 (see the bottom panels of Figures 2 and 3A1–3A2):  $E_p$  sometimes showed shifts by several keV within 0.1–9.5 hr to higher energies and moved back in comparable timescales.

#### 4. CONCLUSIONS AND DISCUSSION

##### 4.1. X-Ray and MWL Flux Variability

###### 4.1.1. Variability Character

The 0.3–10 keV brightness of the source reached the highest level in the time interval 2018 January–February and Mrk 421 was brighter only during the giant outburst in 2013 April. A similar situation was observed in the VHE energy range: the highest VHE states were recorded in 2018 January (coinciding those in the XRT band), while the strongest VHE flare was observed in 2013 April. The TeV-band variability mostly showed a good correlation with the X-ray one, although there were some exceptions (see Figure 6 and Section 4.2). Conversely, there were significantly fewer detections with 5 $\sigma$  significance and/or lower fluxes in the BAT-band, compared to the periods 2005 December–July, 2008 March–July, 2009 October–November, 2010 January–May, 2011 September (see a more detailed discussion in Section 4.3.5).

In other spectral ranges, Mrk 421 exhibited a relatively different behaviour. Namely, the highest 0.3–300 GeV flux from the weekly-binned LAT data was  $(2.2 \pm 1.8) \times 10^{-7} \text{ ph cm}^{-2} \text{ cm}^{-1}$  (in 2016 February, not coinciding with the highest X-ray states). Contrary to the X-ray and VHE observations, significantly higher levels were recorded in 2012 July–August (with the highest historical MeV–GeV level) and the comparable states - in 2013 March and 2014 April. There was a frequent absence or weakness of the correlation between the LAT-band and X-ray variability (Kapanadze et al. 2016, 2017a).

In the UVW1–UVW2 bands, the highest states, corresponding to the de-reddened and host-subtracted fluxes of 23.3–29.8 mJy, were observed during 2016 January–February, and they were significantly lower 2 yr later when the source showed its highest X-ray activity. The higher UV states were observed in 2010 June–2011 April, 2012 April–May, 2012 December–2013 April (the highest historical UV brightness, preceding the giant X-ray outburst), 2013 November–2014 April, 2015 February–June. A nearly-similar situation was found in the optical V-R and OVRO bands.

We checked the MWL data of Mrk 421 for periodicity during 2015 December–2018 April. As an example, Figure 11 presents the LSP and WWZ plots from the XRT observations performed in Intervals 1–3. No

this energy range, similar to the radio–UV and GeV–TeV ranges. Periodic brightness variations have not been found also by different authors (see, e.g., Carnerero et al. 2017; Sandrinelli et al. 2017).

As in past years, the source showed a double-humped behaviour in the plane  $\log \nu - F_{\text{var}}$  during the entire 2015 December–2018 April period and its separate intervals (with  $F_{\text{var}}$ , calculated using the entire data set obtained in the given spectral band during the particular period; see Figures 12A1–12A4 and Kapanadze et al. 2016, 2017a, 2018a,b). We used the 1-d binned XRT, BAT, FACT, OVRO and optical-UV data in our study, while the 3-d binned LAT was used in the 0.3–300 GeV energy range (similar to the light curves provided in Figure 6). Although the latter binning and the cuts at 3 $\sigma$ –5 $\sigma$  detection significances can lead to some undersampling in the corresponding  $F_{\text{var}}$  values, a two-humped shape with the synchrotron and higher-energy peaks situated at the X-ray and VHE frequencies, respectively, seems to be inherent for HBLs and are frequently reported for these sources. For our target, a similar result was reported by various authors from various MWL campaigns (Aleksic et al. 2015a,b; Ahnen et al. 2016; Abeysekara et al. 2017), favouring the one-zone SSC model (predicting the correlated X-ray–VHE variability) for Mrk 421 in different shorter-term periods and indicating that the electron energy distribution is most variable at the highest energies (Aleksic et al. 2015b).

Although the optical data points in Figures 12A1–12A2 violate the general trend of increasing variability power from radio to hard X-ray frequencies, this result can be related to the data sampling: some V and R-band observations were carried out at Arizona Observatory in those time intervals when the source was not targeted by UVOT, although it was showing a strong variability. The presence of lower VHE peaks in Figures 12A1–12A3, compared to the peak in the synchrotron frequency, is difficult to explain via the upscattering of synchrotron photons in the Thomson regime (when a squared relation is expected). However, this result can be related to the use of the FACT excess rates instead the linear fluxes in our study.

###### 4.1.2. Flux Lognormality

We also checked whether the X-ray and MWL fluxes of Mrk 421, observed in the 2015 December–2018 April time interval, showed lognormal distributions. According to McHardy (2008), a lognormal flux behavior in blazars can be indicative of the variability imprint of the accretion disk onto the jet. Moreover, the lognormal fluxes have fluctuations, that are, on average, proportional to the flux itself, and are indicative of an underlying multiplicative, rather than additive physical process. Consequently, the excess variance  $\sigma_{\text{excess}}^2 = \sqrt{S^2 - \sigma_{\text{err}}^2}$  (with the quantities  $S$  and  $\sigma_{\text{err}}^2$  defined in Equation (3)) plotted versus the



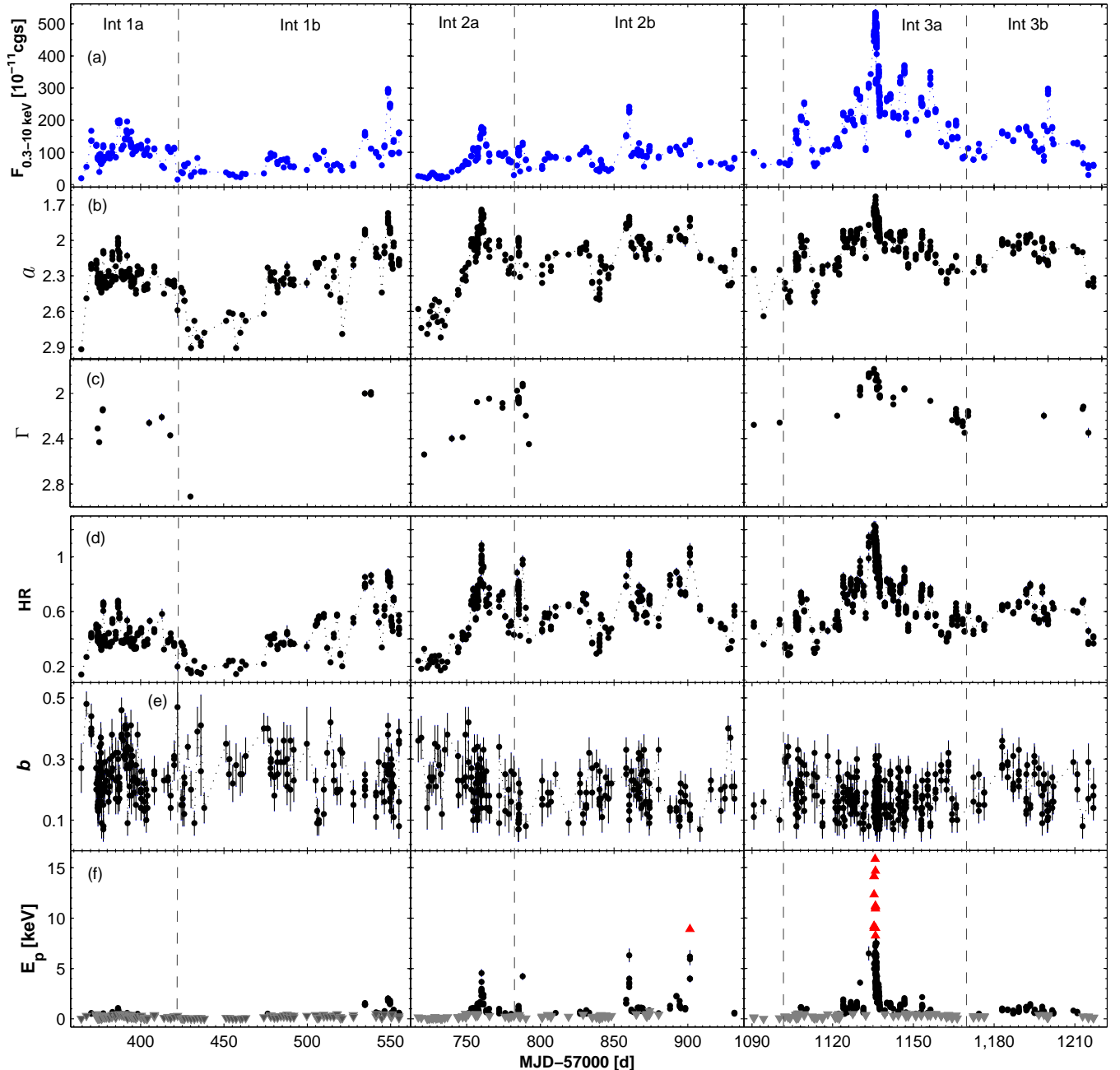


**Figure 10.** De-absorbed 0.3–10 keV flux and different spectral parameters plotted versus time. The gray and red triangles in the bottom panel indicate the upper and lower limits to the intrinsic position of the synchrotron SED peak, respectively.

trend (Chevalier et al. 2019).

For BLLs, the lognormality in different spectral ranges and time intervals were reported for PKS 2155–304, BL Lac and 1ES 1011+496 (Chevalier et al. 2019; Giebels & Degrange 2009; Sinha et al. 2017). In the case of Mrk 421, the lognormality was studied by Sinha et al. (2017) using the radio, optical–UV and LAT-band data obtained during 2009–2015. The lognormal fit to the histograms were clearly preferred for most of the bands, leading to the suggestion that the flux variability in the source can be mainly attributed to changes in the particle spectrum rather than to the variability of the jet physical parameters such as the magnetic field or Doppler factor (see Sinha et al. 2016).

In order to investigate lognormality, we fit the histograms of the MWL fluxes with the Gaussian and lognormal functions (similar to the aforementioned studies). Figure 13A1 demonstrates, that the distribution of the de-absorbed 0.3–10 keV flux from the entire 2015 December–2018 April period is closer to the lognormal shape than the Gaussian one (similar to the MAXI

observations; Figure 13B). A lognormal behaviour is confirmed by the corresponding scatter plot in the  $\sigma_{\text{excess}}^2 - \overline{F}_{0.3-10\text{keV}}$  plane where the data points, corresponding to the XRT-band flares during 2015 December–2018 April, show an increasing linear trend with higher mean flux (Figure 13H1). Note that this result is mainly due to the observations performed in Intervals 1 and 3, while the data from Interval 2 are closer to the Gaussian function (Figures 13A2–13A6).

The longer-term flares may result from the propagation and evolution of relativistic shocks through the jet (see Sokolov et al. 2004 and references therein). The shock appearance can be related to the instabilities occurring in the accretion disk, which may momentarily saturate the jet with extremely energetic plasma with much higher pressure than the steady jet plasma downstream (Sokolov et al. 2004). Consequently, a lognormal flaring activity of the source on longer timescales may indicate a variability imprint of the accretion disk onto the jet. However, the fluxes, corresponding to the high-

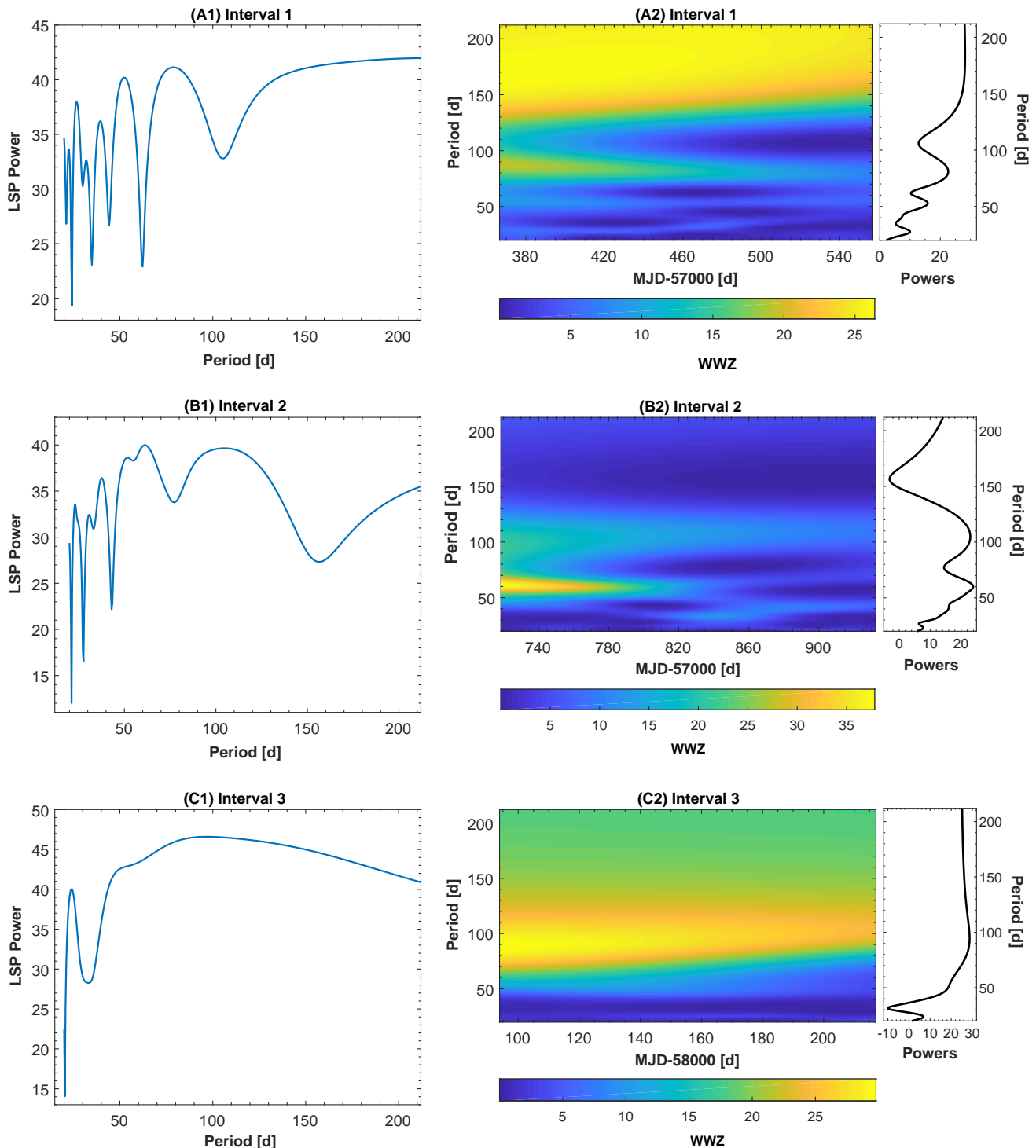


**Figure 11.** The LSP and WWZ plots from the XRT observations of Mrk 421 in different intervals.

est X-ray states in Intervals 1 and 3, produce outliers from the lognormal distributions. These states generally were recorded during fast flares superimposed on the long-term one. These flares could be triggered by the shock interaction with the jet inhomogeneities whose origin was related to the jet instabilities (e.g., strong turbulent structures; Marscher 2014). Therefore, no lognormal distribution of those fluxes is expected in that case, owing to the absence of the AD variability imprint. Moreover, Interval 2 clearly shows a better fit to the Gaussian function and since this period was characterized, on average, by lower X-ray states (see Section 3.1 and Table 3), this result could be related to the propagation of weaker shocks through the jet. On the other hand, a shock weakness possibly was due to the lower AD variability in that period, which resulted in a fewer imprint onto the jet of

Mrk 421.

In each interval, the FACT and LAT-band fluxes clearly showed a better fit of the lognormal function with the corresponding distributions (Figures 13C1–13D4). Although the same is shown by the  $R$ -band histogram constructed for the entire 2015 December–2018 April period, it is impossible to draw a firm conclusion related to the lognormal behaviour of the source in this band, since we could not construct the corresponding  $\overline{F}_R - \sigma_{\text{excess}}^2$  scatter plot due to the sparse sampling of the optical flares (see Figure 6). In contrast, the OVRO data do not show a good fit between the corresponding histogram and lognormal function. This result implies the radio-contributions from various emission regions with different physical conditions. Finally, the UVOT-band histograms show a better (but not good) fit with the lognormal function compared

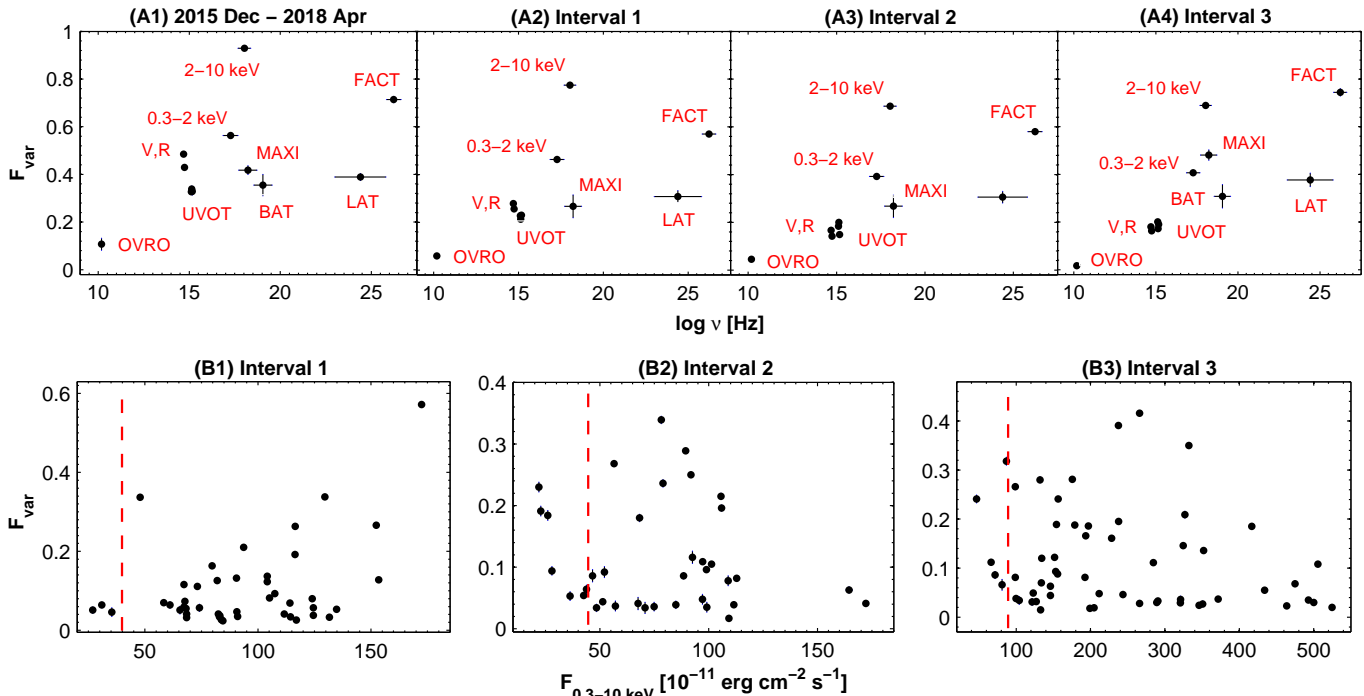


**Figure 12.** Panels (A1)–(A4): multi-instrument fractional amplitude  $F_{var}$  as a function of the energy in different periods; panels (B1)–(B3):  $F_{var}$  of the 0.3–10 keV IDVs as a function of the flux in different periods. In each plane, a vertical, red dashed line represents the threshold below which the low X-ray states were observed (see the text for the quantitative definition)

to the Gaussian one only in Interval2 (see the bottom row of Figure 13).

#### 4.1.3. Intraday Variability

In the 2015 December–2018 April period, the source showed three intraday flux-doubling and three flux-halving events with  $\tau_d=14.2$ – $17.8$  hr and  $\tau_h=4.8$ – $18.9$  hr, respectively. Note that the flux doubling time can be used for constraining the upper limit to the emission zone as follows (Saito et al. 2013 and references therein)

$$R_{em} \leq \frac{c\tau_d\Gamma_{em}}{1+z}, \quad (7)$$

with  $R_{em}$  and  $\Gamma_{em}$ , the size and Lorentz-factor of the emission zone, respectively. Adopting the typical value of the bulk Lorentz-factor for the emission zone  $\Gamma_{em}=10$  (Falomo et al. 2014), we obtain upper limits of  $5.0 \times 10^{15}$ – $1.9 \times 10^{16}$  cm for the emission zones with intraday flux-doubling instances. Mrk 421 exhibited more extreme behaviour during the densely-sampled *Swift*-XRT campaign in 2009 May 22–27 (net exposure time of 23.5 ks, 59 orbits)  $\tau_h=1.4$ – $1.5$  hr and  $\tau_d=6.5$ – $12.4$  hr (Kapanadze et al. 2018b). A series of the brightness halving and doubling events with  $\tau_{d,h} \sim 1.1$  hr were recorded on 2009 February 17, and a similar variability occurred also during 2017 February 2–3 (see Section 3.1 and Figure 1i). Note that the successive large brightness drop and rise events can be explained as a consequence of a shock passage through two inhomogeneous areas with strong magnetic fields, which are separated by a region with significantly weaker field and lower particle density (yielding the generation of fewer X-ray photons). The most extreme behaviour was observed during the giant X-ray outburst in 2013 April, with several events showing  $\tau_d=1.2$ – $7.2$  hr and  $\tau_h=1.0$ – $3.5$  hr (Kapanadze et al. 2016).

The distribution of the 0.3–10 keV fluxes extracted from those *Swift*-XRT pointings which showed IDVs in the period 2015 December–2018 April is not well fitted with the lognormal function, in contrast to the longer-term flares. This result hints at the absence of an AD variability imprint onto these events. Moreover, Fig-

low X-ray states<sup>19</sup> when the IDVs caused by the instability in AD or in the inner jet regions should be more easily detectable: the variable emission from these regions will not be “overwhelmed” by the huge flux produced near the shock front, propagating through the jet and causing longer-term flares (see Mangalam & Wiita 1993 and references therein). On the other hand, most of these events are detected from short XRT exposures and the entire cycle (brightness increase and drop) is generally not recorded, in contrast to the longer-term flares. Therefore, it is not possible to draw a firm conclusion about the absence of lognormality. However, the 0.3–10 keV flux values from those IDVs whose complete variability cycles were observed do not exhibit a lognormal flux distribution. Therefore, these results favour the “shock-in-jet” scenario where IDVs are triggered by the interaction of a shock front with small-size jet inhomogeneities (Sokolov et al. 2004; Marscher 2014; Mizuno et al. 2014).

The duty cycle of the 0.3–10 keV IDVs (i.e., the fraction of total observation time during which the object displayed IDVs; see Romero et al. 1999 and references therein) amounted to 58.4%, which is higher than that shown by the source in 2009–2012 and 2013 November–2015 June (43–46 per cent; Kapanadze et al. 2017a, 2018b), but significantly lower than compared to the periods 2005–2008 and 2013 January–May (about 84%; Kapanadze et al. 2016, 2018a). Note that this result can be partially related to significantly more densely sampled campaigns in some parts of the latter periods. For example, Mrk 421 was observed very densely during 2006 June 15–25 with a total exposure of 119 ks distributed over 124 *Swift*-XRT orbits.

On the other hand, the source exhibited an unequal 0.3–10 keV activity on intraday timescales in different epochs. Note that the XRT pointings without IDVs were mainly performed during the lower X-ray states. However, we also discerned some flares

<sup>19</sup> The de-absorbed 0.3–10 keV flux values, corresponding to the low X-ray states of the source, were below the thresholds of about  $4.0 \times 10^{-10}$  cgs,  $4.5 \times 10^{-10}$  cgs and  $9.0 \times 10^{-10}$  cgs in Intervals 1, 2 and 3, respectively.

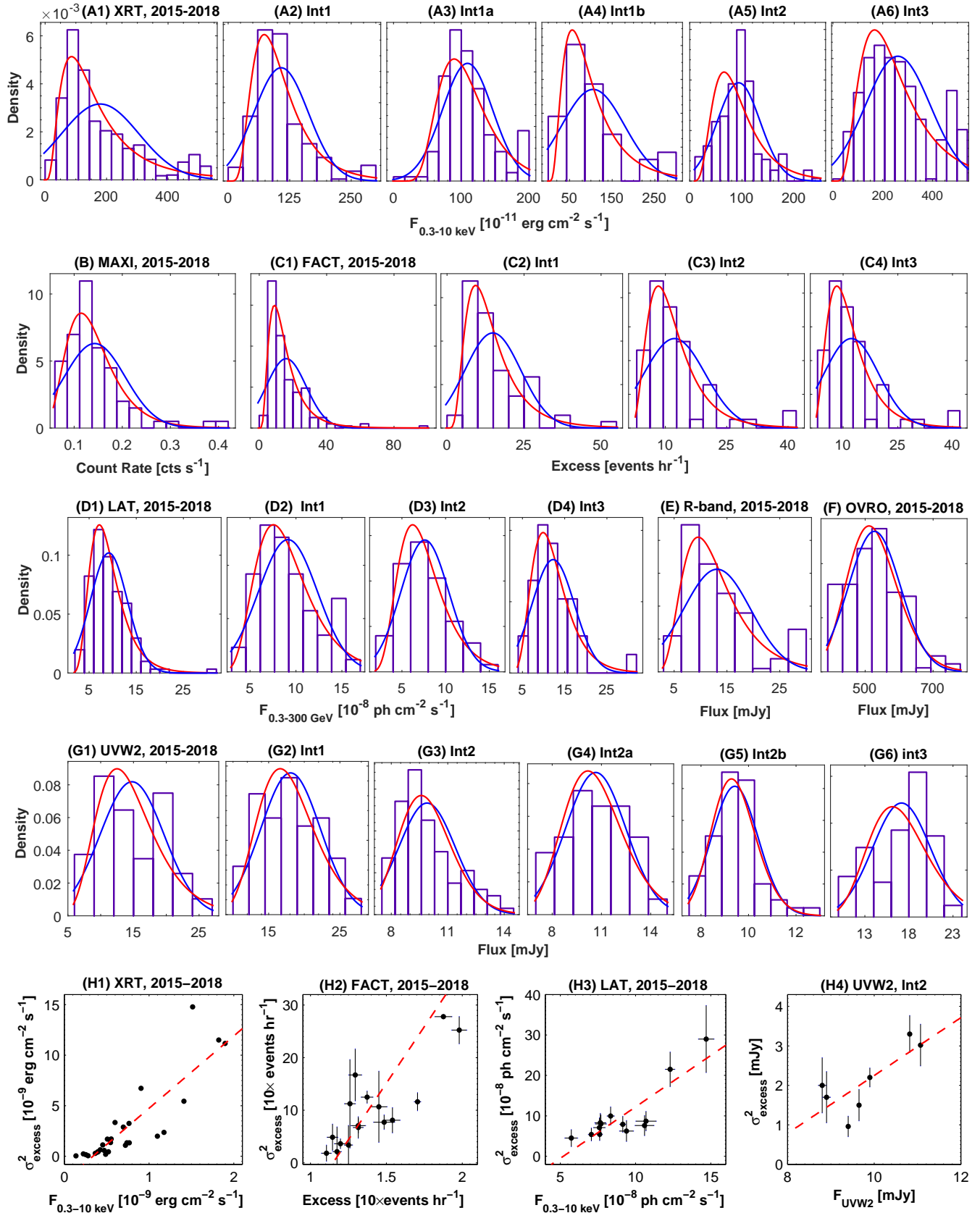


**Figure 13.** Histograms of the MWL fluxes. In each plot, red and blue lines correspond to the lognormal and Gaussian fits, respectively. For the space reason, the period 2015 December–2018 April is denoted as “2015–2018” in the plot titles. The bottom row: scatter plots with  $\sigma_{\text{excess}}^2$  and the average flux for the MWL data. A linear fit is shown in red dashed line.

with a clear lack of intraday activity. For example, such flaring activity was observed during MJD 57521–548 with  $CR_{\text{max}}=95.73\pm 0.32\text{ctss}^{-1}$ , which is a factor of 2.5 higher than the mean rate during the whole period 2015 December–2018 April. This event was preceded by the long time interval (MJD 57400–57520)

when the source had showed the lowest mean rate ( $23.24\pm 0.01\text{ctss}^{-1}$ ) and duty cycle of IDVs (36%) for the entire 2015–2018 period. A similar situation was observed in 2010 June–July when the source demonstrated low 0.3–10 keV states with  $CR\sim 10\text{ctss}^{-1}$  and insignificant variability over 1.5 months, possibly related to the

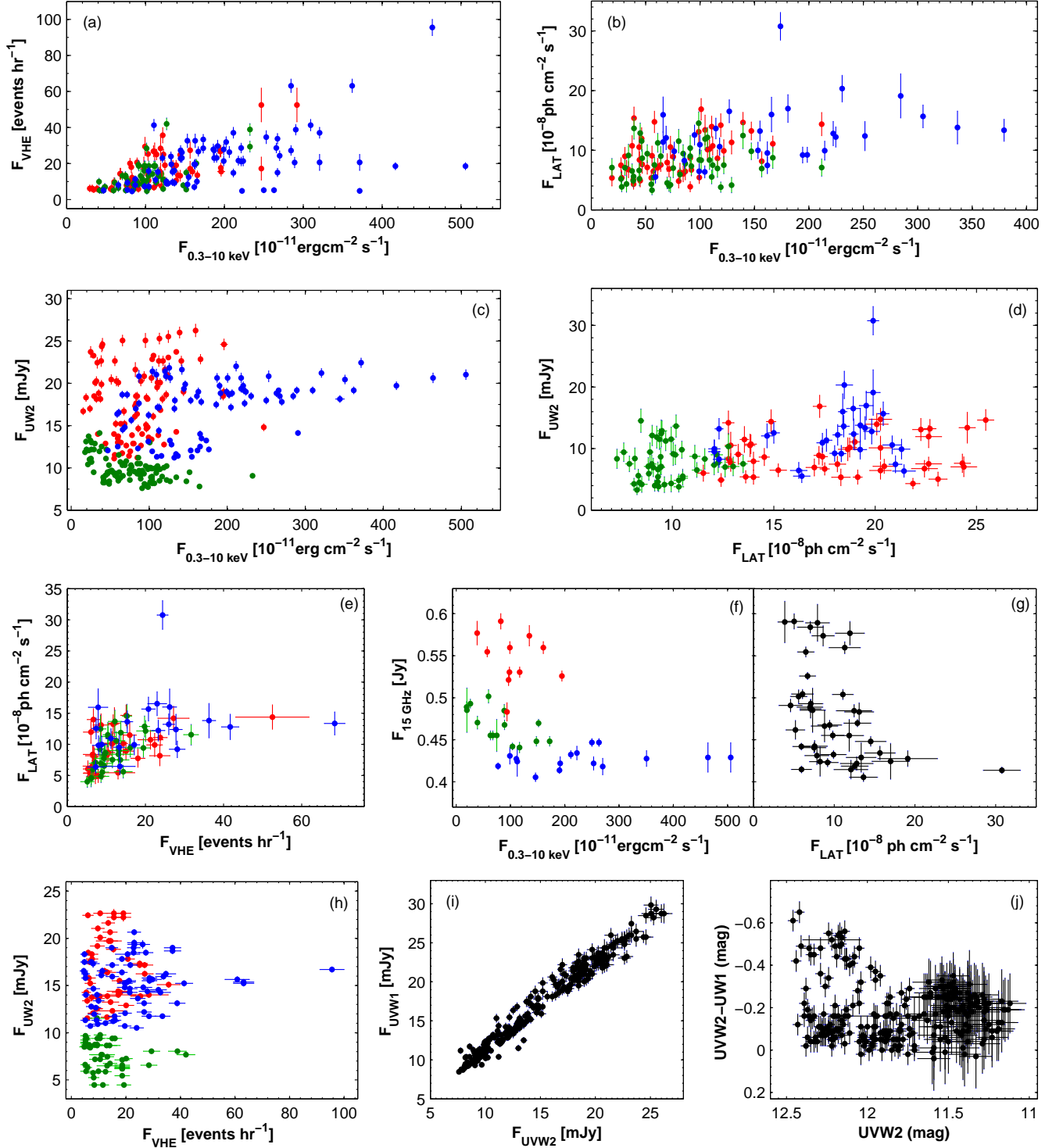


**Figure 14.** Correlations between the MWL fluxes. The coloured points in Figures 14a–14h correspond to the different periods as follows: red – Interval 1, green – Interval 2, blue – Interval 3.

absence of strong shock waves, which could cause a long-term flare in different spectral bands (Kapanadze et al. 2018b). Moreover, the source also showed significantly slower and weaker IDVs during those densely-sampled XRT observations presented in Figure 4. These results lead to the conclusion that the source underwent weaker variability on intraday timescales during the low X-ray states and some longer-term flares.

The last column of Table 4 provides a list of the variable spectral factor presumably making the dominant contribution to the particular 0.3–10 keV IDV. The most common factor in the observed fast variability was a change of the photon index (i.e., in the slope of the Particle Energy Distribution, PED). Neverthe-

less, some events were related to the transition from a log-parabolic PED into a power-law one and/or vice versa. The most extreme log-parabolic/power-law/log-parabolic transitions occurred within the 1-ks exposures during ObsID 31202174 (MJD 58135.39), 4-th orbit of ObsID 31202175 (MJD 58136.33) and first orbit of ObsID 31202178 (MJD 58137.11), in the epoch of the strongest X-ray flaring activity of the source during 2015–2018. Such extreme events can be related to very fast variability of the magnetic field properties within the jet regions which are smaller than  $R=10^{14}$  cm (for  $\delta=10$ ): a transition from a magnetic field characterized by decreasing confinement efficiency with rising electron’s gyroradius or strong turbulence (both yielding a log-parabolic

PED) into a volume without these properties and vice versa (see below). A number of the IDVs were related also to the variability of the curvature parameter, the position and height of the synchrotron SED peak. The changes of the latter two quantities imply an intraday and even a subhour variability of the physical parameters (magnetic field, Doppler factor,  $\gamma_{3p}^2$ : the peak of the function  $n(\gamma)\gamma^3$ ) included in the relations as follows (Rybicki & Lightman 1979 and references therein)

$$E_p \propto \gamma_{3p}^2 B \delta, \quad S_p \propto N \gamma_p^2 B^2 \delta^4. \quad (8)$$

#### 4.2. Multiwavelength Correlations

During the time interval presented in this work, the TeV-band variability showed the strongest correlation with the X-ray one: strong VHE flares or enhanced activity mostly coincided with strong X-ray flares (see Section 3.2). Consequently, Figure 14a shows a positive  $F_{0.3-10\text{keV}}-F_{\text{VHE}}$  correlation in each interval, although it was relatively weak in Interval3 compared to that in Interval1 (the difference between the values of the coefficient  $\rho$  was larger than the corresponding error ranges; see Table 11). In fact, some data points from Interval3 make the largest exceptions from the general trend. Such situation was particularly evident during MJD 58145–153 (Interval3a): the VHE flux showed a decline by a factor of  $\sim 4$  and subsequent low states during the fast X-ray flare with one of the highest states during the 2015–2018 period (see Figure 6a). Two data points in the right lower corner of the  $F_{0.3-10\text{keV}}-F_{\text{VHE}}$  plane belong to the X-ray flare around MJD 58136 when the 0.3–10 keV flux reached its highest values, while the TeV-band state was the highest on the previous day. This situation is hard to reconcile with one-zone SSC scenarios (Blazejowski et al. 2005). However, Fig 7a demonstrates that no strictly simultaneous XRT observation was performed during those 20-min FACT pointings detecting the source in the highest VHE states. Therefore, we cannot draw any firm conclusion for this case.

The source was not detectable with  $3\sigma$  or showed low VHE states when it had undergone short-term X-ray flares during MJD (57)413–422 (Figure 6c), MJD (57)425–438 and MJD (57)473–491 (Figure 6d), MJD (57)723–730 and MJD (57)801–838 (Figure 6e). Similar instances were reported from the FACT observations of Mrk 421 performed in previous years (Kapanadze et al. 2016, 2017a). Moreover, the MWL campaign in 2002 December–2003 January revealed a strong X-ray flare by a factor of 7 within 3 d, not accompanied by a comparable TeV-counterpart (Rebillot et al. 2006). The TeV flux reached its peak days before the X-ray flux during the giant flare in 2004 that was impossible to explain via the standard one-zone SSC model, and Blazejowski et al. (2005) suggested this as an instance of the “orphan” TeV flare. Acciari et al. (2011) also found high X-ray states, not accompanied by TeV flaring and vice versa in 2006–2008. We conclude that the broadband SED can not always be modelled using one-zone SSC scenarios, although they were acceptable for Mrk 421 during the majority of the X-ray flares (corroborated by the appearance of a two-hump structure in the  $F_{\text{var}}-\log\nu$  plane, with the peaks at X-ray and TeV frequencies, respectively).

The 0.3–10 keV variability showed a weak positive correlation with that observed in the MeV–GeV energy range (see Figure 14b and Table 11). The source did not undergo comparable LAT-band activity or exhibited lower states during the most extreme X-ray behaviour (MJD 58145–58160, Figure 6a). Moreover, the

**Table 11**

Correlations between the MWL fluxes (denoted by “ $F_i$ ” for the particular  $i$ -band in Column 1) during different periods. In Cols (2)–(3),  $\rho$  and  $p$  stand for the Spearman coefficient and the corresponding p-chance, respectively.

Quantities	$\rho$	$p$
2015 Dec–2018 Apr		
$F_{0.3-2\text{ keV}}$ and $F_{2-10\text{ keV}}$	0.93(0.02)	$< 10^{-15}$
$F_{0.3-10\text{ keV}}$ and $F_{\text{FACT}}$	0.61(0.08)	$5.44 \times 10^{-10}$
$F_{0.3-10\text{ keV}}$ and $F_{\text{UVW2}}$	0.30(0.11)	$4.07 \times 10^{-5}$
$F_{0.3-10\text{ keV}}$ and $F_{\text{UVW1}}$	0.25(0.11)	$8.34 \times 10^{-4}$
$F_{0.3-10\text{ keV}}$ and $F_{\text{LAT}}$	0.49(0.10)	$1.03 \times 10^{-8}$
$F_{0.3-10\text{ keV}}$ and $F_{15\text{ GHz}}$	-0.53(0.09)	$8.89 \times 10^{-9}$
$F_{\text{UVW2}}$ and $F_{\text{UVW1}}$	0.94(0.02)	$< 10^{-15}$
$F_{\text{UVW1}}$ and $F_{\text{UVW2}}$	0.96(0.01)	$< 10^{-15}$
$F_{\text{UVW2}}$ and $F_{\text{LAT}}$	0.32(0.11)	$7.58 \times 10^{-5}$
$F_{\text{FACT}}$ and $F_{\text{LAT}}$	0.55(0.09)	$1.24 \times 10^{-9}$
$F_{\text{LAT}}$ and $F_{15\text{ GHz}}$	-0.49(0.14)	$3.55 \times 10^{-4}$
$F_{0.3-2\text{ GeV}}$ and $F_{2-300\text{ GeV}}$	0.75(0.06)	$5.02 \times 10^{-13}$
Int 1		
$F_{0.3-2\text{ keV}}$ and $F_{2-10\text{ keV}}$	0.88(0.03)	$< 10^{-15}$
$F_{0.3-10\text{ keV}}$ and $F_{\text{FACT}}$	0.62(0.07)	$1.28 \times 10^{-11}$
$F_{0.3-10\text{ keV}}$ and $F_{\text{LAT}}$	0.44(0.10)	$6.10 \times 10^{-8}$
$F_{\text{FACT}}$ and $F_{\text{LAT}}$	0.45(0.10)	$3.71 \times 10^{-8}$
Int 1a		
$F_{0.3-10\text{ keV}}$ and $F_{\text{UVW2}}$	0.56(0.11)	$5.01 \times 10^{-5}$
$F_{0.3-10\text{ keV}}$ and $F_{\text{UVW1}}$	0.48(0.12)	$7.79 \times 10^{-5}$
Int 1b		
$F_{0.3-10\text{ keV}}$ and $F_{\text{UVW2}}$	-0.46(0.11)	$6.77 \times 10^{-5}$
$F_{0.3-10\text{ keV}}$ and $F_{\text{UVW1}}$	-0.43(0.11)	$3.40 \times 10^{-5}$
Int 2		
$F_{0.3-2\text{ keV}}$ and $F_{2-10\text{ keV}}$	0.93(0.02)	$< 10^{-15}$
$F_{0.3-10\text{ keV}}$ and $F_{\text{FACT}}$	0.51(0.09)	$7.76 \times 10^{-9}$
$F_{0.3-10\text{ keV}}$ and $F_{\text{UVW2}}$	-0.45(0.09)	$1.08 \times 10^{-6}$
$F_{0.3-10\text{ keV}}$ and $F_{\text{UVW1}}$	-0.47(0.09)	$2.03 \times 10^{-7}$
$F_{0.3-10\text{ keV}}$ and $F_{\text{LAT}}$	0.34(0.12)	$3.17 \times 10^{-4}$
$F_{0.3-10\text{ keV}}$ and $F_{15\text{ GHz}}$	-0.71(0.09)	$3.33 \times 10^{-9}$
$F_{\text{FACT}}$ and $F_{\text{LAT}}$	0.64(0.08)	$6.10 \times 10^{-11}$
Int 2a		
$F_{0.3-10\text{ keV}}$ and $F_{\text{UVW2}}$	-0.75(0.09)	$1.92 \times 10^{-8}$
$F_{0.3-10\text{ keV}}$ and $F_{\text{UVW1}}$	-0.74(0.09)	$4.56 \times 10^{-8}$
Int 3		
$F_{0.3-2\text{ keV}}$ and $F_{2-10\text{ keV}}$	0.93(0.03)	$< 10^{-15}$
$F_{0.3-10\text{ keV}}$ and $F_{\text{FACT}}$	0.45(0.11)	$9.01 \times 10^{-8}$
$F_{0.3-10\text{ keV}}$ and $F_{\text{UVW2}}$	0.39(0.10)	$4.07 \times 10^{-5}$
$F_{0.3-10\text{ keV}}$ and $F_{\text{UVW1}}$	0.38(0.10)	$9.95 \times 10^{-5}$
$F_{0.3-10\text{ keV}}$ and $F_{\text{LAT}}$	0.39(0.11)	$5.26 \times 10^{-4}$

detections or low fluxes were recorded in the time intervals MJD (58)190–215 and (57)364–381 (Figures 6b–6c), MJD (57)731–746 (Figures 6e). An even weaker  $F_{0.3-10\text{keV}}-F_{0.3-300\text{GeV}}$  correlation was observed during 2009–2012 and 2013 January–June, while no significant correlation was found for the period 2013 November–2015 June (Kapanadze et al. 2016, 2017a, 2018b).

We extracted the 0.3–2 GeV and 2–300 GeV photon fluxes from the LAT observations to check their cross-correlation and search for possible contributions from different electron populations to the LAT-band emission. We used 2-weekly binned observations to ensure  $N_{\text{pred}} \geq 10$  (Table 12). Figure 15a exhibits a strong  $F_{0.3-2\text{GeV}}-F_{2-300\text{GeV}}$  correlation, demonstrating a predominantly common origin for the soft and hard LAT-band photons. This result is in contrast to that obtained for 1ES 1959+650 during the period 2016 August–2017 November, with a weak correlation between the softer and harder LAT-band fluxes that hints at uncorrelated behaviour and possible contribution from different particle populations (Kapanadze et al. 2018e).

Note that the LAT-band flux was also correlated weakly with the UVOT- and FACT-band fluxes, respectively (see Figures 14d–14e). This result can be explained

energies in the Thomson regime (a similar relation between the X-ray and VHE photons). Another source of the LAT-band emission can be an upscatter of X-ray photons in the Klein-Nishina (K-N) regime. An upscatter of the BAT-band photons in the same regime could be the case during those time intervals when the source showed low VHE states with the absent  $F_{0.3-10\text{keV}}-F_{\text{VHE}}$  correlation or was not detectable in the TeV energy range (owing to strong suppression of the  $\gamma$ -ray emission in this regime; see Tramacere et al. 2009).

Both LAT and XRT-band fluxes showed an anti-correlation with the 15 GHz emission which was particularly strong in Interval 2 in the case of the X-ray emission (see Figures 14f–14g and Table 11). A similar situation is evident from the scatter plot  $F_{0.3-10\text{keV}}-F_{\text{UVW2}}$  constructed for Interval 2 and Interval 1b (Figure 14c and the aforementioned table). Such a feature was reported also by Aleksic et al. (2015b) and explained through a hardening of the electron energy distribution that can shift the entire synchrotron bump to higher energies. Consequently, the emission of the synchrotron SED in the radio–UV energy range is expected to decrease with rising X-ray brightness. Note that such MWL behaviour is expected for the stochastic acceleration of electrons within the specific initial conditions (see Section 4.3).

No  $F_{0.3-10\text{keV}}-F_{\text{UVW2}}$  correlation at the 99% confidence level was detected in Interval 1, and a very weak positive correlation occurred in Interval 3. An anti-correlation was observed also during 2009–2012, and uncorrelated variabilities occurred in 2005–2008 and 2014 February–2015 June (Kapanadze et al. 2017a, 2018b). A stronger positive correlation was observed during 2013 January–June and 2013 November–2014 January (Kapanadze et al. 2016, 2017a). We have not found a correlation between the UV and VHE fluxes, hinting at an insignificant role for the upscatter of the UV photons to VHE frequencies in the Thomson regime (Figure 14h). Finally, the UVW1–UVW2 fluxes showed very strong cross-correlations, as in previous periods, reflected in the absence of the UV colour variability and demonstrating the generation of these photons by the same electron population via the synchrotron mechanism in each period (Figures 14i–14j).

### 4.3. Spectral Properties and Particle Acceleration Processes

#### 4.3.1. First-Order Fermi Acceleration

A positive  $a$ – $b$  correlation (see Figure 9a), detected in Intervals 1–3, shows an importance of the first-order Fermi acceleration since this correlation was predicted for those jet regions where particles are confined by a magnetic field at the shock front, whose confinement efficiency is declining with increasing gyration radius (i.e., particle’s energy; so-called EDAP: energy-dependent acceleration probability process; Massaro et al. 2004). Consequently, the probability  $p_i$  that a particle undergoes an acceleration step  $i$ , with the corresponding energy  $\gamma_i^q$  and energy gain  $\varepsilon$ , is given by  $p_i = g/\gamma_i^q$ , where  $g$  and  $q$  are positive constants. Consequently, the probability of the particle’s acceleration is lower when its energy increases, and the differential energy spectrum is given by  $N(\gamma) \sim \gamma/\gamma_0^{-s-r \log \gamma/\gamma_0}$ , with a linear relationship between the spectral index and curvature terms ( $s$  and  $r$ , respectively)  $s = -r(2/q) \log g/\gamma_0 - (q-2)/2$ . The synchrotron emission produced by this distribution is given by

$$P_S(\nu) \propto (\nu/\nu_0)^{-(a+b \log(\nu/\nu_0))}, \quad (9)$$

with  $a = (s-1)/2$  and  $b = r/4$  (Massaro et al. 2004).

This result can be explained due to the sub-samples having different slopes in the  $a$ – $b$  plane, leading to a large scatter of the data points during the entire period 2015 December–2018 April. Note that some sub-samples showed even a negative  $a$ – $b$  trend (e.g., those corresponding to the short-term flares recorded during MJD 57364–375, 57395–57408, 57527–57544 in Interval 1), which is expected when  $g > \gamma_0$ , i.e., there were electron populations with a very low initial energy  $\gamma_0$  in the emission zone. Moreover, the co-existence of stochastic (second-order Fermi) acceleration also could weaken the aforementioned correlation, since the latter is not expected within the stochastic mechanism. The Monte Carlo simulations of Katarzynski et al. (2006) revealed that electrons can be accelerated at the shock front via EDAP and continue gaining energy via the stochastic mechanism into the shock downstream region (after escaping the shock front). After some time, a particle will be able to re-enter the shock acceleration region and repeat the acceleration cycle. Consequently, such combined acceleration will not result in the strong  $a$ – $b$  correlation.

A stronger positive  $a$ – $b$  correlation was found for our target during the XRT observations in 2005–2008 and 2015 February ( $\rho=0.41$ – $0.57$ ; Kapanadze et al. 2017a, 2018a). An even stronger correlation was reported by Massaro et al. (2004) from the *BeppoSAX* observations in 1997–2000. On the other hand, this correlation was weaker during 2009–2012 ( $\rho=0.21 \pm 0.07$ ) and absent in 2013 January–2014 June (Kapanadze et al. 2016, 2017a).

#### 4.3.2. Stochastic Acceleration and Turbulence

As in previous years, the source mostly showed low curvatures ( $b \sim 0.3$  or smaller for a vast majority of the log-parabolic spectra; see Section 3.3.1), i.e., wider synchrotron SED, expected in the case of efficient stochastic acceleration (Massaro et al. 2011b). This result is related to the inverse proportionality of the PED curvature  $r$  to the diffusion coefficient  $D$  in the Fokker-Plank kinetic equation:  $r \propto D^{-1}$ . On the other hand,  $r \propto \varepsilon/(n_s \sigma_\varepsilon^2)$  (Massaro et al. 2004), with  $n_s$ , the number of the acceleration steps;  $\sigma_\varepsilon^2$ , the variance of the energy gain  $\varepsilon$ . Consequently, the detection of low spectral curvatures implies higher values of  $n_s$  and diffusion coefficient, which needs strongly developed turbulence in smaller acceleration region.

In fact, the relativistic magnetohydrodynamic simulations of Mizuno et al. (2014) showed that shock propagation can strongly amplify the turbulence in the shocked jet material due to its interaction with higher-density inhomogeneities existing in the pre-shock medium; the more frequent detection of the 0.3–10 keV IDVs in flaring X-ray states (compared to quiescence periods; see Section 4.1.3) demonstrates the viability of this scenario for Mrk 421 during the time interval presented in this work. Moreover, our detection of the anti-correlation  $F_{0.3-10\text{keV}}-b$  (see Figure 9c), i.e., a dominance of lower curvatures in higher X-ray states, favours the shock-in-jet scenario and strongly-developed turbulence during those states.

The simulations of Mizuno et al. 2014 also demonstrated that the higher-energy photons (including those having 0.3–10 keV energies) are expected to originate in the smallest jet regions, which contain the strongest magnetic field and yield the most rapid time variability. In fact, the fastest IDVs, occurring within a few hundred seconds, were observed mostly in the highest X-ray states in Interval 3a, and such instances can be related to the interaction of the relativistic shock front with the smallest-

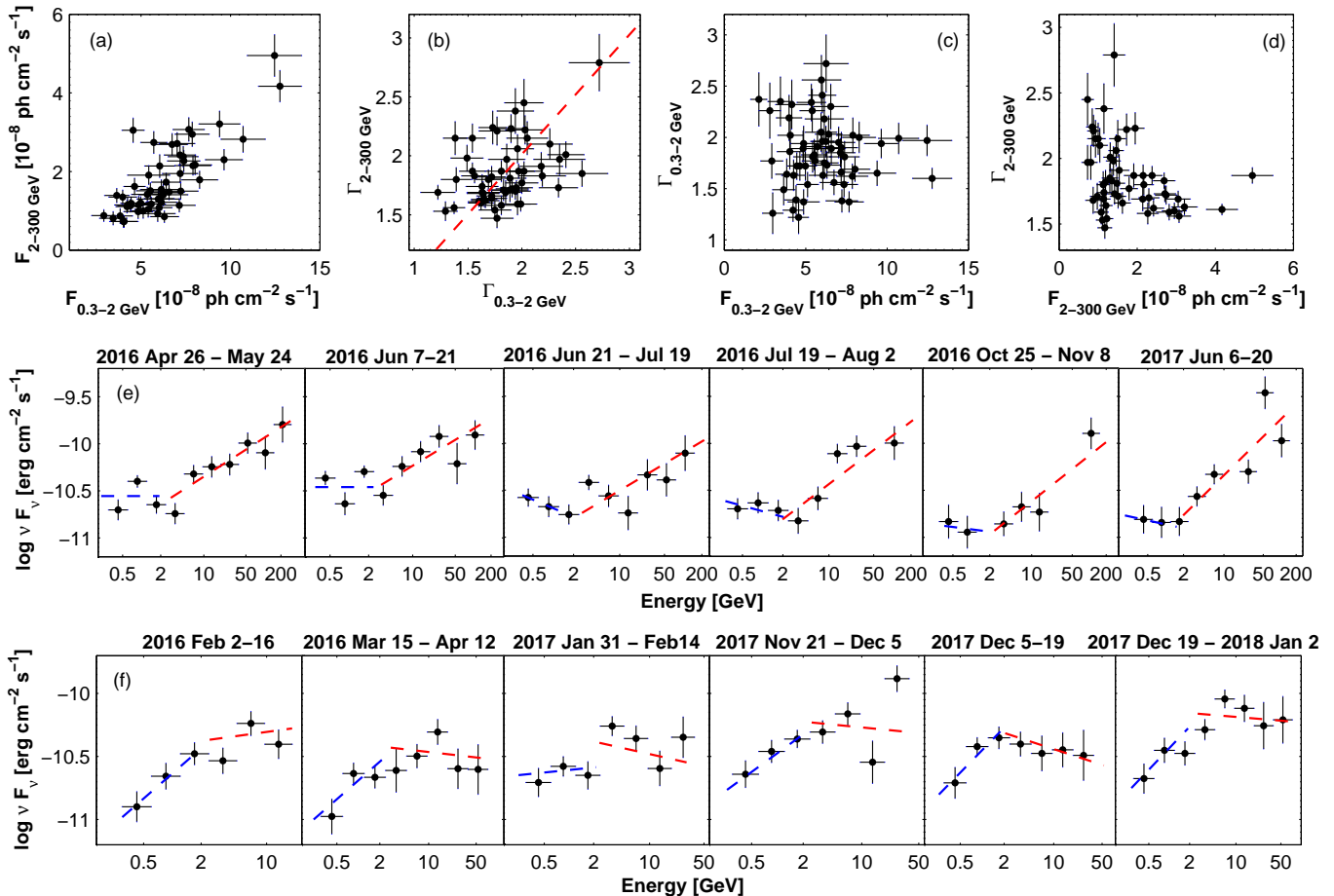


**Figure 15.** Results from 2-weekly-binned LAT data for the period 2015 December–2018 April. The scatter plots: 0.3–2 GeV and 2–300 GeV photon fluxes (panel (a)); 0.3–2 GeV and 2–300 GeV photon indices, with the red dashed line corresponding to  $\Gamma_{0.3-2\text{GeV}} = \Gamma_{2-300\text{GeV}}$  (panel (b)); 0.3–2 GeV photon flux and index (panel (c)); 2–300 GeV photon flux and index (panel (d)). Panels (e) and (f): the 0.3–300 GeV SEDs from the time intervals showing a hardening and softening in the 2–300 GeV energy range, respectively. The blue and red dashed lines represent linear fits to the 0.3–2 GeV and 2–300 GeV SEDs, respectively.

fields (according to light-travel argument). Note also that this sub-interval was remarkable for the lowest mean curvature observed in the whole 2015–2018 time interval, implying the existence of the most efficient stochastic acceleration in that sub-interval.

Along with the flux, the 0.3–10 keV spectral parameters varied on intraday timescales. Sometimes, these changes were extremely fast, within 1-ks observational runs: curvature risings by 0.19–0.22; hardenings by  $\Delta a = 0.08$ –0.23; shifts of the synchrotron SED peak by several keV to higher or lower energies; transitions from the log-parabolic PED into the power-law one and/or vice versa. Such behaviour could be related to the passage of a shock front through the regions with spatial scales  $l \lesssim 10^{14}$  cm and significantly stronger turbulence, separated by the region with less extreme physical properties (magnetic field strength, particle number density, bulk Lorentz factor etc.). Our detections show the viability of the simulations of Mizuno et al. (2014), yielding a strong turbulence amplification on extremely small spatial scales in the shocked jet medium.

Stochastic acceleration scenarios predict the presence of the  $E_p$ – $b$  anti-correlation (Tramacere et al. 2009). However, the latter was not detected at the 99% confidence level in Interval 1 and was weak during Intervals 1–3 (see Table 9 and Figure 9b). This correlation is deduced from the relation  $\ln E \propto 2 \ln \gamma_p + 3/(5b)$  (Tramacere et al. 2009), with  $\gamma_p$ , the PED peak energy. Note that the significant difference in the  $\gamma_p$  values, corresponding to the different X-ray flares, may result in a large scatter of the data points in the  $E_p$ – $b$  plane or even a destruction of the anti-correlation. Furthermore, this correlation is also pre-

dicted for EDAP through  $\log E \sim 3/(10b)$  (Chen 2014), and since this relation shows a different slope compared to the stochastic case, the joint operation of these mechanisms can yield a large scatter in the  $E_p$ – $b$  plane and weaken the anti-correlation.

We found a positive  $F_{0.3-10\text{keV}}-E_p$  correlation during Intervals 1–3, i.e., a trend of shifting the synchrotron SED peak to higher energies with rising X-ray flux (see Figure 9g). Tramacere et al. (2009) demonstrated that as the peak energy of the emission increases, the cooling timescale shortens and can compete with the acceleration timescales. It is then possible to observe a bias in the  $E_p$ – $b$  relation (weakening the anticorrelation), since the cooling timescale is shorter than that of EDAP or stochastic acceleration.

Note that the anti-correlation between the 0.3–10 keV and radio variabilities, discussed above and explained as resulting from the shifting of the PED peak with a rising X-ray flux (corroborated by our finding of the positive  $F_{0.3-10\text{keV}}-E_p$  correlation), is expected in the framework of stochastic acceleration with a narrow initial energy distribution, having the mean energy significantly higher than the equilibrium energy (Katarzynski et al. 2006). Presumably, such a physical condition was not the case for some X-ray flares when no declining radio brightness was observed. Moreover, since there were some flares with a negative  $a$ – $b$  trend, this result hints at the low initial energies of the accelerating particles during those events.

In the case of the low spectral curvature, the electron volume density  $n_e$  is expected to be higher, yielding a brighter IC peak within the SSC scenario (Massaro et al.



**Table 12**

The results from 2-weekly-binned LAT data in the 0.3–2 GeV and 2–300 GeV bands. Cols (2) and (6) present the test-statistics corresponding to Mrk 421 in each band; Cols (3) and (7) – number of the model-predicted photons. The photon fluxes (Cols (4) and (8)) are provided in units of  $10^{-8}$  ph cm $^{-2}$  s $^{-1}$ . Cols (5) and (9) – the 0.3–2 GeV and 2–300 GeV photon indices, respectively. The last column provides a remark related to the interplay between the 0.3–2 GeV and 2–300 GeV spectral hardnesses: 1 – increasing hardness with energy; 2 – harder spectra in the 0.3–2 GeV energy range; 3 – no significant difference between the higher- and lower-energy photon indices. In Col. (8), an asterisk stands for the upper limit to the 2–300 GeV flux.

Dates (1)	0.3–2 GeV				2–300 GeV				Remark (10)
	TS (2)	$N_{pred}$ (3)	Flux (4)	$\Gamma$ (5)	TS (6)	$N_{pred}$ (7)	Flux (8)	$\Gamma$ (9)	
2015-12-08–08-22	55.0	143.5	6.05(0.85)	1.63(0.14)	175.8	24.6	2.14(0.29)	1.69(0.09)	3
2015-12-22–2016-01-05	113.1	380.1	7.67(0.88)	1.37(0.10)	639.9	55.9	3.07(0.30)	1.56(0.05)	2
2016-01-05–01-19	80.5	274.8	9.39(1.15)	1.65(0.12)	481.4	40.4	3.21(0.33)	1.63(0.06)	3
2016-01-19–02-02	80.5	256.1	7.86(0.96)	1.62(0.12)	400.8	37.6	2.95(0.31)	1.60(0.06)	3
2016-02-02–02-16	62.7	183.7	4.56(0.62)	1.22(0.16)	482.6	47.0	3.05(0.31)	1.69(0.06)	2
2016-02-16–03-01	103.0	280.5	8.28(1.02)	2.00(0.15)	257.0	28.6	1.79(0.22)	1.77(0.09)	3
2016-03-01–03-15	51.4	143.9	4.64(0.60)	1.72(0.14)	247.3	22.4	1.62(0.21)	1.66(0.08)	3
2016-03-15–03-29	43.2	108.5	3.65(0.69)	1.49(0.15)	178.0	20.1	1.39(0.18)	1.98(0.11)	2
2016-03-29–04-12	57.7	136.5	4.41(0.71)	1.39(0.14)	153.8	18.0	1.13(0.16)	1.80(0.10)	2
2016-04-12–04-26	61.9	144.0	5.40(0.76)	2.26(0.21)	95.4	16.2	1.04(0.20)	2.10(0.13)	2
2016-04-26–05-10	58.6	166.9	6.02(0.72)	1.96(0.12)	126.2	13.4	1.08(0.18)	1.59(0.09)	1
2016-05-10–05-24	60.5	179.6	7.39(0.91)	1.81(0.15)	274.3	23.3	2.27(0.27)	1.58(0.08)	3
2016-05-24–06-07	80.4	208	6.41(0.82)	2.03(0.18)	216.3	28.1	1.73(0.23)	2.22(0.12)	3
2016-06-07–06-21	110.6	353.7	9.64(1.04)	1.94(0.14)	334.2	33.4	2.30(0.26)	1.70(0.07)	1
2016-06-21–07-05	44.3	101.1	6.14(1.18)	2.18(0.20)	111.0	14.3	1.54(0.25)	1.91(0.12)	1
2016-07-05–07-19	46.7	99.8	5.97(1.20)	2.56(0.24)	144.9	13.5	1.30(0.20)	1.85(0.11)	1
2016-07-19–08-02	64.8	156.6	5.57(0.80)	1.77(0.15)	177.9	17.2	1.17(0.18)	1.47(0.08)	1
2016-08-02–08-16	37.7	106.2	6.54(1.08)	2.30(0.22)	66.4	7.7	1.54*	-	-
2016-08-16–08-30	39.7	109.5	3.84(0.69)	1.64(0.15)	86.7	11.2	0.87(0.19)	1.68(0.10)	3
2016-08-30–09-13	36.7	70.2	2.92(0.68)	1.77(0.17)	118.2	13.9	0.88(0.15)	2.21(0.12)	2
2016-09-13–09-27	25.9	31.5	2.12(0.50)	2.37(0.26)	38.4	6.7	1.32*	-	-
2016-09-27–10-11	28.0	56.7	4.15(1.00)	2.32(0.24)	6.1	3.2	1.56*	-	-
2016-10-11–10-25	22.9	75.7	2.98(0.63)	1.26(0.20)	65.5	8.3	1.61*	-	-
2016-10-25–11-08	32.1	55.3	3.45(0.77)	2.35(0.24)	81.6	9.9	0.81(0.17)	1.97(0.13)	1
2016-11-08–11-22	67.0	168.4	5.52(0.78)	1.83(0.15)	223.4	23.2	1.51(0.20)	1.71(0.09)	3
2016-11-22–12-06	55.0	201.8	5.12(0.67)	1.54(0.12)	103.4	13.4	1.00(0.19)	2.15(0.12)	2
2016-12-06–12-20	35.1	69.5	6.25(1.37)	2.72(0.28)	87.6	10.5	1.41(0.28)	2.79(0.24)	3
2016-12-20–2017-01-03	75.1	187.2	6.57(0.87)	1.89(0.15)	175.1	21.6	1.48(0.20)	1.81(0.10)	3
2017-01-03–01-17	94.8	246.7	7.90(1.01)	2.02(0.17)	317.0	33.0	2.15(0.24)	1.87(0.08)	3
2017-01-17–01-31	61.7	186.3	6.14(0.86)	1.75(0.15)	155.7	15.4	1.22(0.16)	1.54(0.08)	3
2017-01-31–02-14	89.7	205.9	7.19(0.99)	1.90(0.15)	262.1	29.9	1.95(0.23)	2.23(0.12)	2
2017-02-14–02-28	69.3	217.0	5.72(0.74)	1.91(0.15)	393.7	43.7	2.74(0.28)	1.72(0.07)	3
2017-02-28–03-14	46.2	111.8	4.02(0.78)	1.86(0.17)	72.3	10.7	0.73(0.15)	1.97(0.13)	3
2017-03-14–03-28	63.6	195.6	6.31(0.80)	1.73(0.13)	90.2	10.9	0.85(0.15)	2.24(0.14)	-
2017-03-28–04-11	73.2	210.9	4.45(0.58)	1.72(0.13)	212.2	24.4	1.19(0.16)	1.82(0.09)	2
2017-04-11–04-25	100.5	301.6	8.03(0.92)	1.69(0.12)	331.6	34.1	2.17(0.25)	1.80(0.08)	3
2017-04-25–05-09	58.4	164.5	4.98(0.69)	1.72(0.14)	176.1	17.6	1.20(0.16)	1.64(0.09)	2
2017-05-09–09-23	46.1	112.5	4.25(0.72)	1.63(0.15)	123.7	15.5	1.15(0.18)	1.74(0.10)	3
2017-05-23–06-06	48.5	111.2	5.94(0.98)	2.05(0.19)	70.0	9.8	0.93(0.20)	2.15(0.14)	3
2017-06-06–06-20	50.5	90.2	3.98(0.78)	2.19(0.22)	216.3	22.3	1.35(0.18)	1.83(0.09)	2
2017-06-20–07-04	26.7	39.5	2.80(0.66)	2.26(0.27)	35.9	5.2	1.42*	-	-
2017-07-04–07-18	31.1	98.6	4.87(0.97)	1.37(0.12)	71.3	6.4	1.82*	-	-
2017-07-18–08-01	75.8	171.7	6.24(0.83)	1.96(0.15)	194.0	23.2	1.46(0.19)	2.06(0.12)	3
2017-08-01–08-15	49.6	107.7	4.06(0.78)	2.02(0.18)	76.6	11.4	0.73(0.15)	2.45(0.20)	2
2017-08-15–08-29	49.6	121.7	4.84(0.80)	1.89(0.17)	112	12.7	0.98(0.18)	1.71(0.10)	3
2017-08-29–09-12	52.1	141.5	4.22(0.62)	1.29(0.11)	149.4	16.6	1.11(0.16)	1.53(0.08)	2
2017-09-12–09-26	83.8	195.2	7.14(0.90)	1.85(0.14)	126.4	17.0	1.14(0.17)	1.69(0.10)	3
2017-09-26–10-10	49.0	114.7	5.35(0.88)	2.34(0.18)	223.0	23.1	1.42(0.18)	1.73(0.08)	1
2017-10-10–10-24	58.0	134.7	4.87(0.80)	1.94(0.17)	98.5	13.8	1.15(0.22)	2.38(0.19)	2
2017-10-24–11-07	67.4	173.9	5.43(1.18)	1.81(0.15)	280.7	29.9	1.91(0.24)	1.87(0.09)	3
2017-11-07–11-21	84.1	147.2	6.02(0.84)	2.41(0.17)	216.2	24.2	1.31(0.17)	2.01(0.11)	1
2017-11-21–12-05	96.1	284.1	7.36(0.84)	1.54(0.12)	353.6	38.2	2.38(0.26)	1.87(0.07)	2
2017-12-05–12-19	63.3	248.0	7.22(0.98)	1.38(0.11)	152.5	15.8	1.50(0.21)	2.15(0.14)	2
2017-12-19–2018-01-02	73.8	206.6	6.74(0.87)	1.56(0.12)	387.7	36.2	2.69(0.28)	1.83(0.06)	2
2018-01-02–01-16	98.8	264.9	7.18(0.88)	1.66(0.13)	360.5	41.6	2.42(0.26)	1.62(0.06)	3
2018-01-16–01-30	86.6	279.7	10.71(1.24)	1.99(0.15)	321.5	29.0	2.82(0.33)	1.59(0.06)	1
2018-01-30–01-13	73.8	255.8	12.46(1.52)	1.97(0.15)	386.0	37.3	4.95(0.53)	1.87(0.06)	3
2018-02-13–02-27	161.5	587.7	12.77(1.21)	1.60(0.10)	748.9	65.5	4.17(0.40)	1.61(0.04)	3
2018-02-27–03-13	86.4	208.6	7.02(1.01)	1.95(0.15)	434.1	42.5	2.71(0.28)	1.73(0.06)	1

2011b). Since the source generally shows its IC peak at the TeV frequencies (see, e.g., Acciari et al. 2011), lower VHE states are expected along with the high spectral curvatures. In fact, during the majority of the XRT observations with  $b > 0.4$ , Mrk 421 was not detectable with  $3\sigma$  significance with FACT or showed excess rates lower

than the mean value during 2015 December–2018 April. However, there were two exceptions showing higher VHE states along with  $b > 0.4$  (MJD 57388 and 57548). On the other hand, the source was not detectable or showed low VHE states during some time intervals with predominantly low curvatures (e.g., MJD 57408–57486, 58147–

58162). These instances demonstrate that the one-zone SSC scenario was not always acceptable for our target in the here-presented period.

#### 4.3.3. Spectral Loops

In the Bohm limit, the first-order Fermi mechanism yields an electron acceleration timescale  $\tau_{\text{FI}} \approx 10200(c/v_{\text{sh}}^2)\sqrt{\gamma^2 - 1}(B/1\text{G})^{-1}$ , with  $v_{\text{sh}}$  – the shock speed (Tammy & Duffy 2009). For a 1-G field, relativistic shock ( $v_{\text{sh}} \rightarrow c$ ) and  $\gamma \lesssim 10^4$ , this timescale will be a few milli-seconds or shorter. In that case, the acceleration and injection of electrons into the emission zone will be instantaneous and a clockwise (CW) evolution of the X-ray flare in the plane  $F_{0.3-10\text{keV}}\text{-HR}$  is expected, making the spectrum progressively harder in the brightening phase of the source, due to the emergence of a flaring component starting at hard X-rays (Tramacere et al. 2009). Although the de-absorbed soft 0.3–2 keV and hard 2–10 keV fluxes showed strong or very strong cross-correlations during Intervals 1–3 (Figure 16a and Table 11), the latter underwent a higher variability in each interval (see Table 3 for the corresponding  $F_{\text{var}}$  and  $\mathcal{R}$  values) and the hysteresis patterns were clearly evident in the  $F_{0.3-10\text{keV}}\text{-HR}$  plane. The CW loops, expected in the case of EDAP, are evident in Figures 16c–16n, 16p, 16r–16u during the various short and longer-term flares discussed in Section 3.1. Two CW-loops were detected also on intraday timescales (Figures 16w and 16y).

However, EDAP can not be considered as instantaneous in the case of significantly weaker magnetic fields, frequently inferred from the one or multi-zone SSC modelling of Mrk 421 ( $B \lesssim 0.05\text{G}$ ; see, e.g., Abeysekara et al. 2017; Aleksic et al. 2012). Furthermore, no instantaneous injection is expected for the hadronic content in the emission zone whose acceleration time-scales are  $\sim 1000$ -times longer than for electrons (Tammy & Duffy 2009). Note that the latter is more naturally compatible with the hard  $\gamma$ -ray spectra characterized by the photon index  $\Gamma \lesssim 1.8$  (Shukla et al. 2016; Mannheim 1993), and such spectra frequently were recorded during the LAT observations in the here-presented period (as hard as  $\Gamma_{\text{min}} = 1.26 \pm 0.13$ ). Consequently, EDAP will be more gradual than instantaneous, X-ray flares propagate from low energies to high energies and counter-clockwise (CCW) spectral evolution should be observed (Tammy & Duffy 2009). Such behaviour was also frequently observed in Intervals 1–3 (see Figures 16b–16e, 16g–16j, 16o–16t, 16v). Note that the slow, gradual acceleration and CCW-loops are also expected during the stochastic acceleration in the jet region with low magnetic field and high matter density (Virtanen & Vainio 2005). On the contrary, this time-scale can be much shorter and even instantaneous in the purely or mainly leptonic plasma if the matter density is low and high magnetic fields are presented. In such situation, CW-type loops can develop, although this requires quite ideal turbulence conditions with particle-scattering waves moving in opposite directions over a sufficiently long length-scale (Tammy & Duffy 2009).

#### 4.3.4. Power-law Spectra

Along with EDAP and stochastic mechanisms, there could be other “competing” processes acting in the emission zone and weakening the observed  $E_{\text{p}}\text{-}b$  correlation. Namely, the first-order Fermi process can yield a power-law PED when the magnetic field properties are variable and its confinement efficiency becomes independent of the

of the 0.3–10 keV spectra showed a simple power-law distribution of the photons with frequency, and they were observed mostly in higher X-ray states. This percentage was unprecedented high during 2005–2008 (27.5%) and the power-law spectra were observed most frequently during the densest XRT campaign in 2006 June 15–25, although they were recorded in any brightness states shown by the source in that period (Kapanadze et al. 2018a). A higher percentage (13%) and no clear trend with brightness was observed also during 2013 January–May (Kapanadze et al. 2016). On the contrary, the periods 2009–2012 and 2013 November–2015 June were characterized by significantly fewer occurrence of power-law spectra (4.9%–6.7%; Kapanadze et al. 2017a, 2018b).

Hard power-law PEDs with slopes  $p < 2$  can be established by relativistic magnetic reconnection, expected to operate efficiently in highly-magnetized plasma with the magnetization parameter  $\sigma \gtrsim 10$  (Sironi & Spitkovsky 2014). However, the simulated broadband SEDs, obtained by Petropoulou et al. (2016) for the cases  $\sigma = 10\text{--}50$ , differ significantly from those of Mrk 421 constructed using the data obtained during the different MWL campaigns (Abeysekara et al. 2017; Balokovic et al. 2016; Aleksic et al. 2012 etc.), particularly, in the MeV–TeV energy range.

#### 4.3.5. The Position of the Synchrotron SED Peak and Variable Turbulence Spectrum

During 2015 December–2018 April, only 15% of the spectra showed  $E_{\text{p}} > 2\text{keV}$ , i.e., peaking at the hard X-ray frequencies (taking into account the error ranges). This percentage is significantly lower than that shown by Mrk 421 during 2005–2008 (24%; Kapanadze et al. 2018a) and a higher occurrence of such spectra were recorded also during 2009–2012 (17%; Kapanadze et al. 2018b). Note that the spectra with  $E_{\text{p}} > 2\text{keV}$  were mostly concentrated in the sub-periods 2006 April–July, 2008 March–June, 2009 November, 2010 January–May. Due to the position of the synchrotron SED peak at higher frequencies, BAT detected the source with  $5\sigma$  confidence frequently in the aforementioned time intervals: the BAT-band photons are generally of synchrotron origin in the HBL sources and no significant contribution from the IC photons are found, in contrast to the low-energy-peaking BLLs (LBLs; e.g., OJ 287; see Kapanadze et al. 2018c).

On the other hand, the periods 2013 January–May and 2013 November–2015 June were characterized by a significantly lower occurrence of hard X-ray peaking spectra (2% and 5%, respectively; see Kapanadze et al. 2016, 2017a). Note that the percentage of the spectra with  $E_{\text{p}} > 2\text{keV}$  was significantly higher for 1ES 1959+650 in 2016 January–August (48%) and 2016 August–2017 November (28%) (Kapanadze et al. 2018d,e). The highest value of this parameter was  $12.80 \pm 0.86\text{keV}$ . However, more extreme case with 94% spectra with the synchrotron peaks in X-rays was recorded for Mrk 501 during the extended X-ray flaring activity in 2014 March–October (Kapanadze et al. 2017b). In that period, the maximum value  $E_{\text{p}}^{\text{max}} = 20.96 \pm 2.81\text{keV}$  and unprecedented spectral behaviour when the synchrotron SED peak position underwent a shift by at least two orders of frequency and moved beyond 100 keV (Tavecchio et al. 2001). For our target, the most extreme SED position was observed on 2006 April 22 with  $E_{\text{p}}^{\text{max}} = 26_{-8}^{+19}\text{keV}$ , obtained by Tramacere et al. (2009) from the joint fit of the log-parabolic model with the XRT and BAT spectra. Al-

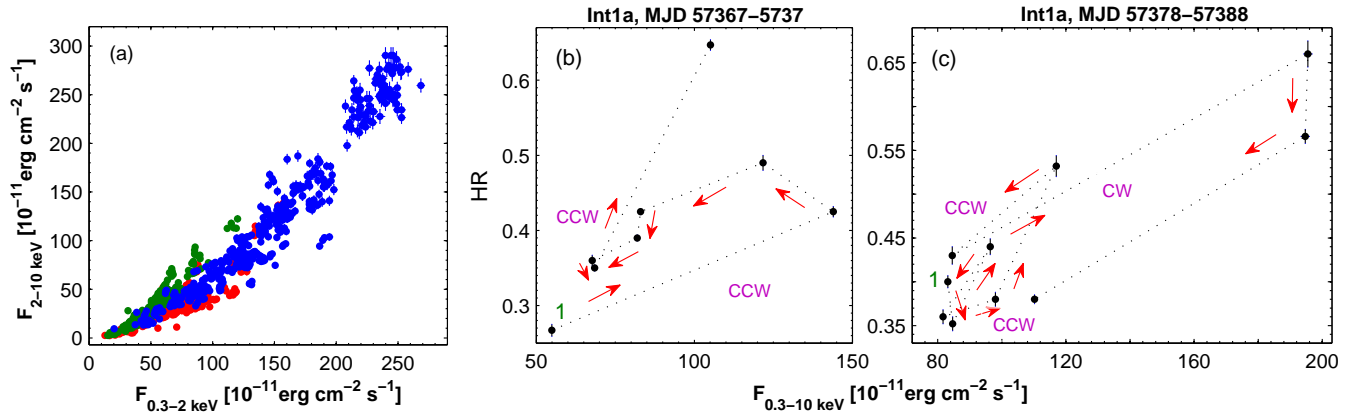


**Figure 16.** Panel (a): scatter plot with de-absorbed 0.3–2 keV and 2–10 keV fluxes. The subsequent panels: spectral hysteresis patterns in different sub-intervals (extract; available in its entirety in machine-readable form). In each HR-flux plane, the start point is denoted by “1”.

$E_p > 100$  keV from the 2006 April–June observations, our thorough analysis of these spectra showed insignificant spectral curvature and a good fit with a simple power-law (Kapanadze et al. 2018a).

Fig. 9h demonstrates a positive  $\log E_p$ – $\log S_p$  correlation with a slope of  $0.63 \pm 0.08$  – the value of the exponent  $\alpha$  in the relation  $S_p \propto E_p^\alpha$ . This relation was predicted by the simulations of Tramacere et al. (2011) corresponding to the case when the momentum-diffusion coefficient  $D$  is variable during stochastic acceleration of the X-ray emitting electrons. Consequently, there should be a transition from the Kraichnan spectrum of the turbulence with the exponent  $Q=3/2$  into the “hard sphere” spectrum ( $Q=2$ ). In the latter regime, the scattering and acceleration timescales are independent of the particle energy. During the transition, the synchrotron SED follows the expectation of a lower curvature for the harder turbulence spectra (Tramacere et al. 2011). On average, the lowest curvatures were observed in Interval 3 which shows the strongest  $\log E_p$ – $\log S_p$  correlation during 2015 December–2018 April (see Table 9). This results can serve as another confirmation of the stochastic acceleration of particles in that period.

#### 4.3.6. LAT-Band Spectral Properties and Possible Jet-Star Interaction

The photon indices corresponding to the softer  $\Gamma_{0.3-2\text{GeV}}$  and harder  $\Gamma_{2-300\text{GeV}}$  LAT-bands showed a weak cross-correlation during 2015 December–2018 April (see Figure 15b and Table 9). On some occasions, the index  $\Gamma_{2-300\text{GeV}}$  was lower than the 0.3–2 GeV one, which can be related to the soft gamma ray excess at energies of several hundred MeV. One of the possible explanations consists in a star-jet interaction, expected in the blazars hosted by elliptical galaxies (including Mrk 421; see Scarpa et al. 2000). These galaxies may have a population of red giants surrounding the blazar jet and can carry large wind-blown bubbles into the jet, leading to gamma-ray emission through bubble-jet interactions (Torres-Alba & Bosch-Ramon 2019). Note that those instances, characterized by a spectral hardening with energy, are mostly observed in the period 2016 April–August, while no opposite spectral trend was observed during that time (see Figure 15e and Table 12). The simulations of Torres-Alba & Bosch-Ramon (2019) have shown that the IC emission, resulting from the jet-bubble interaction, is negligible ( $L_{\text{IC}} \sim 10^{40}$  erg s $^{-1}$ ), while that generated by the synchrotron mechanism can make a significant contribution to the MeV energy budget ( $L_{\text{IC}} \sim 10^{44}$  erg s $^{-1}$ ; see Aleksic et al. 2012 for comparison). In the latter case, the equipartition value of the magnetic field,  $B_{\text{eq}} \sim 0.1$  G, is required.

required.

In 17 cases, the index  $\Gamma_{2-300\text{GeV}}$  was higher than its lower-energy “counterpart” (the data points situated below the red dashed line in Figure 15b; see Figure 15f for the corresponding SEDs). These cases could be related to the up-scatter of X-ray photons to the 2–300 GeV energy range in the K–N regime, yielding a steepening of the corresponding photon spectrum with respect to that established in the 0.3–2 GeV range by means of the Thompson up-scattering of the optical–UV photons (Kapanadze et al. 2018e). Finally, 8 out of 23 LAT-band SEDs, where the difference between the  $\Gamma_{0.3-2\text{GeV}}$  and  $\Gamma_{2-300\text{GeV}}$  photon indices did not exceed the error ranges, were very hard and their origin could be related to the hadronic contribution to the 0.3–300 GeV energy range (as suggested by Shukla et al. 2016).

## 5. SUMMARY

In this paper, we have presented the spectral and timing results obtained during the intensive *Swift*-XRT and MWL observations of Mrk 421 in 2015 December–2018 April. The main results of our study are as follows:

- Similar to the previous years, the source exhibited strong and erratic X-ray variability (without any quasi-periodicity). The most extreme behaviour was recorded during 2017 December–2018 February when a long-term flare, lasting more than 2 months, was superimposed by short-term ones during which the 0.3–10 keV flux exceeded a level of  $5 \times 10^{-9}$  erg cm $^{-2}$  s $^{-1}$ , similar to that recorded on 2008 June 12, and even higher states were observed during the giant outburst in 2013 April. This period was also characterized by several intraday flux doubling and halving events with  $\tau_d = 4.8$ –18.9 hr, as well as by numerous lower-amplitude 0.3–10 keV IDVs with  $F_{\text{var}} = 0.20$ –0.42, including extremely fast brightness fluctuations by 5%–18% within 180–600 seconds. Six another long-term flares of comparable durations but with lower amplitudes were evident during other parts of the period presented in this work.
- The highest VHE states were recorded in 2018 January (coinciding with those in the XRT band) and the TeV-band variability mostly showed a good correlation with the X-ray one, although there were several exceptions when the VHE flux showed a decline or low states during the fast X-ray flare, or the X-ray and VHE peaks were separated by the time interval of  $\sim 1$  d or longer, posing problems for one-zone SSC scenarios. In other spectral ranges, Mrk 421 exhibited a relatively different be-

correlation and the highest 0.3–300 GeV states were recorded about 2-yr earlier than the X-ray ones, while the source exhibited only a moderate LAT-band flaring activity along with the strongest X-ray flares recorded in Interval 3a. Similarly, the highest optical–UV states were observed during 2016 January–February, and they were significantly lower 2 yr later when the source showed its highest X-ray activity. Consequently, the latter was anti-correlated with the UVOT-band variability, and a similar  $F_{0.3-10\text{keV}}-F_{15\text{GHz}}$  relation was observed during the entire 2015 December–2018 April period. Such MWL variability favours some earlier simulations of the second-order Fermi process, when a population of the accelerating electrons are characterized by a narrow initial distribution of energy, having a mean value significantly higher than the equilibrium energy.

- During Intervals 1 and 3, the distributions of the de-absorbed 0.3–10 keV flux showed lognormality features, which could be indicative of the variability imprint of AD on the jet. However, the data from Interval 2 and the highest X-ray states did not show the same property. Since Interval 2 clearly shows a better fit with the Gaussian function and since this period was characterized, on average, by lower X-ray states (see Section 3.1 and Table 3), a lack of the lognormality could be related to weaker shocks through the jet compared to other periods (possibly, due to weaker AD instabilities). The FACT and LAT-band fluxes showed lognormality features in all intervals, in contrast to the radio–UV observations. The 0.3–10 keV IDVs were observed significantly more frequently during higher X-ray states and did not exhibit a lognormality. This result favours the “shock-in-jet” scenario. The longer-term flares may result from the propagation and evolution of relativistic shocks through the jet. The shock appearance could be related to an abrupt increase of the collimation rate at the jet base owing to some processes in the accretion disc, yielding a lognormal flaring behaviour on longer timescales.
- Along with the strong flux variability, the source also exhibited an extreme spectral behaviour. The 0.3–10 keV spectra generally showed their best fits with the log-parabolic model, yielding wide ranges of the curvature parameter  $b=0.07(0.05)-0.48(0.04)$  and photon index at 1 keV  $a=1.63(0.03)-2.92(0.02)$ . The position of the synchrotron SED peak underwent extreme variability on various timescales between the energies  $E_p < 0.1$  keV (the UV frequencies) and  $E_p > 15$  keV, with 15% of the spectra peaking at hard X-rays. The synchrotron SED showed a positive correlation with the 0.3–10 keV flux: it shifted by several keV to higher energies during the flaring phases and moved back along with brightness drops, exhibiting the most violent intraday variability by several keV during the strongest X-ray flares. 33% of the spectra were harder than  $a=2$ , and the energy spectral shape generally followed a “harder-when-brighter” trend (except for some short time intervals with the opposite trend, explained by the emergence of a new soft X-ray component in the emission zone). The photon index varied on diverse timescales with variations from  $\Delta a=0.08-0.23$  within 0.13–0.28 hr to  $\Delta a=0.66-1.07$  in 3–27 d. 9.6% of the spectra were fitted well with a simple power-law, with photon indices  $\Gamma=1.79-2.01$ , but most of them followed

“harder-when-brighter” trend. The source mostly showed a low spectral curvature ( $b \sim 0.1-0.3$ ) and an anti-correlation  $E_p-b$ , as predicted for the efficient stochastic acceleration of X-ray emitting electrons by the magnetic turbulence. Moreover, the source showed a positive  $a-b$  correlation, expected within the EDAP scenario, although it was weak, possibly due to the “competition” with other types of the acceleration mechanisms and cooling processes, not displaying the same correlation.

- The 0.3–10 keV spectra showed a relation  $S_p \propto E_p^\alpha$ , with  $\alpha \sim 0.6$  which demonstrates a transition from the Kraichnan-type turbulence spectrum into the “hard sphere” one, due the variability of the momentum-diffusion coefficient. This result corroborates the importance of stochastic acceleration in the here-presented period. Our study of the spectral hysteresis patterns in the flux–HR plane shows the patterns of both the instantaneous injection and the gradual acceleration of X-ray emitting electrons, owing to first and second-order Fermi processes.
- The source frequently showed very hard 0.3–300 GeV spectra, predicted for a hadronic contribution to the HE emission. On some occasions, the corresponding SED showed a soft  $\gamma$ -ray excess, possibly owing to the jet interaction with a wind-blown bubble from a nearby red giant. This suggestion is corroborated by the fact that the MeV-excess SEDs mostly belong to the period 2016 April–August. On the contrary, there was a softening in the 2–300 GeV energy range compared to the 0.3–2 GeV spectrum, possibly due to the upscatter of X-ray photons in the 2–300 GeV energy range in the K-N regime. This may yield a steepening of the corresponding photon spectrum with respect to the 0.3–2 GeV range, corresponding to the Thompson up-scatter of the optical–UV photons.

PR acknowledges the contract ASI-INAF I/004/11/0. We acknowledge the use of public data from the *Swift* data archive. This research has made use of the XRTDAS software, developed under the responsibility of the ASDC, Italy, and the data from the OVRO 40-m monitoring program which is supported in part by NASA grants NNX08AW31G and NNX11A043G, and NSF grants AST-0808050 and AST-1109911. We thank the FACT collaboration for making their analysis results publicly available. Finally, we thank the anonymous referee for his/her useful comments and suggestions that helped to improve the quality of the paper.

## REFERENCES

- Abdo, A. A., et al. 2011, *ApJ*, 736, 131  
 Abeysekera, A. U., et al. 2017, *ApJ*, 834, 2  
 Acciari, V. A., et al. 2011, *ApJ*, 738, 25  
 Acero, F., et al. 2015, *ApJS*, 218, 23  
 Ahnen, M. L., et al. 2016, *A&A*, 593, 91  
 Alecsic, J., et al. 2012, *A&A*, 542, 100  
 Alecsic, J., et al. 2015a, *A&A*, 578, 22  
 Alecsic, J., et al. 2015b, *A&A*, 576, 176  
 Anderhub, H. et al. 2013, *Journ. of Instr.*, 8, article id. P06008  
 Atwood, W. B., et al. 2009, *ApJ*, 697, 1071  
 Balocovic, M., et al. 2016, *ApJ*, 819, 156  
 Begelman, M.C., Fabian, A C., & Rees, M. J. 2008, *MNRAS*, 384, L19  
 Barthelmy, S. D., et al. 2005, *Space Sci. Rev.*, 120, 143  
 Blazejowski, M., et al. 2005, *ApJ*, 630, 130  
 Bessel, M. S. 1979, *PASP*, 91, 589

- Breeveld, A. A. et al. 2011, *AIPC*, 1358, 373  
 Burrows, D. N., et al. 2005, *Space Sci. Rev.*, 120, 165  
 Carnerero, M. L., et al. 2017, *MNRAS*, 472, 3789  
 Celotti, A., & Ghisellini, G. 2008, *MNRAS*, 385, 283  
 Cesarini, A., PhD Thesis, Nat. Univ. of Ireland Galway, 2013  
 Chen, L. 2014, *ApJ*, 788, 179  
 Chevalier, J. et al. 2019, *MNRAS*, 484, 749  
 Cui, W. 2004, *ApJ*, 605, 662  
 Dermer, C. D., Schlickeiser, R., & Mastichiadis, A., 1992, *A&A*, 256, 27  
 Dorner, D. et al. 2015, *astro-ph/1502.02582*  
 Falomo, R., et al. 2014, *A&A Rev.*, 2014, 22, 37  
 Fitzpartick, E. L., & Messa, D. 2007, *ApJ*, 663, 320  
 Foster, G. 1996, *AJ*, 112, 1709  
 Fukugita, M., et al. 1995, *PASP*, 107, 945  
 Gehrels, N., et al. 2004, *ApJ*, 611, 1005  
 Giebels, B., et al. 2002, *ApJ*, 571, 763  
 Giebels, B., & Degrange, B. 2009, *A&A*, 503, 797  
 Grossmann, A., & Morlet, J. 1984, *SIAM J. Math. Anal.*, 15, 723  
 Kapanadze, B., et al. 2016, *ApJ*, 831, 102  
 Kapanadze, B., et al. 2017a, *ApJ*, 848, 103  
 Kapanadze, B., et al. 2017b, *MNRAS*, 469, 1655  
 Kapanadze, B., et al. 2018a, *ApJ*, 854, 66  
 Kapanadze, B., et al. 2018b, *ApJ*, 858, 68  
 Kapanadze, B., et al. 2018c, *MNRAS*, 480, 407  
 Kapanadze, B., et al. 2018d, *MNRAS*, 473, 2542  
 Kapanadze, B., et al. 2018e, *ApJS*, 238, 13  
 Kalberla, P. M. W., et al. 2005, *A&A*, 440, 775  
 Katarzynski, K., et al. 2006, *A&A*, 453, 47  
 Lomb, N. R. 1976, *Ap&SS*, 39, 447  
 Macomb, N., et al. 1995, *ApJ*, 449, L99  
 Mangalam, A. V., & Wiita P. J. 1993, *ApJ*, 406, 420  
 Mannheim, K. 1993, *A&A*, 269, 60  
 Marscher, A. P., & Gear, W. K. 1985, *ApJ*, 298, 114  
 Marscher, A. P. 2014, *ApJ*, 780, 87  
 Massaro, E., et al. 2004, *A&A*, 413, 489  
 Massaro, F., et al. 2011a, *ApJS*, 197, 24  
 Massaro, F., et al. 2011b, *ApJ*, 742, L32  
 Matsuoka, M., et al. 2009, *PASJ*, 61, 999  
 Mattox, J. R., et al. 1996, *ApJ*, 461, 396  
 McHardy, I. 2008, in *Blazar Variability across the Electromagnetic Spectrum*, Workshop Proc. (Trieste: PoS), 14  
 Mizuno, Y., et al. 2014, *MNRAS*, 439, 3490  
 Moretti, A., et al. 2005, in Siegmund O., ed., *Proc. SPIE Vol. 5898, In-flight Calibration of the Swift XRT Point Spread Function*. SPIE, Bellingham, p. 360  
 Nilsson, K., et al. 2007, *A&A*, 475, 199  
 Padovani, P., & Giommi, P. 1995, *ApJ*, 444, 567  
 Page, M., et al. 2013, *MNRAS*, 436, 1684  
 Petropoulou, M., et al. 2016, *MNRAS*, 462, 3325  
 Pian, E., et al. 2014, *A&A*, 570, 77  
 Poole, T. S., et al. 2008, *MNRAS*, 383, 627  
 Rebillot, P. F., et al. 2006, *ApJ*, 641, 740  
 Richards, J. L., et al. 2011, *ApJ*, 194, 209  
 Romano, P., et al. 2006, *A&A*, 456, 917  
 Romero, G. E., et al. 1999, *A&AS*, 135, 477  
 Roming, P. W. A., et al. 2005, *Space Sci. Rev.*, 120, 95  
 Rybicki, G. B., & Lightman, A. P. 1979, in *Radiative processes in astrophysics* (New York: Wiley-Interscience), 393  
 Saito, S., et al. 2013, *ApJ*, 766, L11  
 Sandrinelli, A., et al. 2017, *A&A*, 600, 132  
 Scargle, J. D. 1982, *ApJ*, 263, 835  
 Scarpa, R., et al. 2000, *ApJ*, 532, 740  
 Shukla, A., et al. 2016, *A&A*, 591, 83  
 Sinha, A., et al. 2016, *A&A*, 591, 81  
 Sinha, A., et al. 2017, *ApJ*, 836, 83  
 Sironi, L., & Spitkovsky, A. 2014, *ApJ*, 783, L21  
 Smith, P. S., et al. 2009, *eConf Proc. C091122*  
 Sokolov, A., et al. 2004, *ApJ*, 613, 725  
 Tavecchio, F., et al. 2001, *ApJ*, 554, 725  
 Tammy, J., & Fuffy, P. 2009, *MNRAS*, 393, 1063  
 Torres-Alba, N., & Bosch-Ramon, V. 2019, *A&A*, 623, 91  
 Tramacere, A., et al. 2009, *A&A*, 501, 879  
 Tramacere, A., et al. 2011, *ApJ*, 739, 66  
 VanderPlas, J. T. 2018, *ApJS*, 236, 16  
 Vaughan, S., et al. 2003, *MNRAS*, 345, 1271  
 Virtanen, J. J. P., & Vainio R. 2005, *ApJ*, 621, 313